Investigation into the catalytic roles of oxygen vacancies during gaseous styrene degradation process via CeO$_2$ catalysts with four different morphologies

Ying Zhang [a,b], Jichang Lu [a,b], Liming Zhang [a,b], Te Fu [a], Jin Zhang [c], Xing Zhu [d], Xiaoya Gao [a,b], Dedong He [b], Yongming Luo [a,b,*], Dionysios D. Dionysiou [e], Wenjie Zhu [a,b,*]

[a] *Faculty of Environmental Science and Engineering, Kunming University of Science and Technology, Kunming 650500, PR China*
[b] *The Innovation Team for Volatile Organic Compounds Pollutants Control and Resource Utilization of Yunnan Province/The Higher Educational Key Laboratory for Odorous Volatile Organic Compounds Pollutants Control of Yunnan Province, Kunming 650500, PR China*
[c] *Yunnan University/Yunnan Key Laboratory of Micro/Nano Materials & Technology, Kunming 650500, PR China*
[d] *Faculty of Metallurgical and Energy Engineering, Kunming University of Science and Technology, Kunming 650093, PR China*
[e] *Environmental Engineering and Science Program, Department of Chemical and Environmental Engineering (ChEE), University of Cincinnati, Cincinnati, OH 45221-0012, USA*

ARTICLE INFO

ABSTRACT

CeO$_2$ catalysts with four different morphologies (sphere, rod, octahedral and cube) were successfully synthesized under hydrothermal conditions and showed quite different thermocatalytic activities for gaseous styrene degradation. Unexpectedly, even though its main exposed lattice plane was (111), spherical CeO$_2$ (CeO$_2$-S), presented the highest styrene catalytic degradation activity (T$_{90}$ =184 ℃) with a styrene degradation rate of 1.36×10^{-3} mol$_{styrene}$ g^{-1} h^{-1} at 200 ℃ that was approximately 12 times higher than that of cubic CeO$_2$. A comprehensive structural characterization and mechanistic study found that the four CeO$_2$ samples exhibit different degrees of lattice distortion and different oxygen vacancy concentrations. CeO$_2$-S has the greatest lattice distortion, resulting in abundant oxygen vacancies. Oxygen vacancies were identified to be the main active sites through increasing reactive oxygen generation. Meanwhile, styrene was activated by adsorption of oxygen vacancies. Based on the results of in-situ DRIFTS and XPS measurements, ^{18}O$_2$ isotope tracing experiment and DFT theoretical calculations, the superior thermocatalytic performance of CeO$_2$-S can be attributed to the lesser accumulation of intermediates on its surface, which follows the Langmuir-Hinshelwood (L-H) mechanism (low temperature) and the Mars-van Krevelen (MVK) mechanism (high temperature). In addition, no obvious decrease was observed in the activity of the CeO$_2$-S catalyst for styrene degradation at 210 ℃ in the presence of water vapor, which is beneficial for the actual industrial application.

1. Introduction

With the rapid economic growth and acceleration of industrial activities and urbanization, environmental pollution, including due to the presence of volatile organic compounds (VOCs), is becoming increasingly severe. VOCs are regarded as a major factor in air pollution because they are precursors of ozone and photochemical smog in the atmosphere [1,2]. Among the typical components of VOCs, styrene is a representative aromatic hydrocarbon (AH) that can harm human health and the environment. Therefore, it is important to effectively control the emission of styrene waste gas [2,3]. In the past few years, several studies

on the treatment of gas-phase styrene by plasma technology [4], photocatalysis [5], thermocatalysis [6,7] and photothermal catalysis [8] have been reported. Among the traditional VOCs treatment methods, low-temperature catalytic oxidation technology is considered to be one of the most feasible and effective methods for the removal of VOCs [9]. Besides, the preparation of catalysts with high activity, high stability and high selectivity is currently an urgent problem in the field of low-temperature catalytic oxidation. The currently used noble metal catalysts are too expensive, while non-precious metal oxide catalysts require high temperatures to achieve effective degradation of volatile organic compounds (VOCs). The preparation of many non-precious

---

metal catalysts such as Ce-based, Co-based and Mn-based oxide catalysts has increasingly become a key focus of catalyst research [10–12].

CeO$_2$ is known as an important, abundant, inexpensive, and stable rare earth material. The Ce atom has highly localized 4 f orbitals that can effectively store electrons [13], and enhance the adsorption and activation of O$_2$ in the gas phase on the CeO$_2$ surface through electron transfer, thereby improving the oxidation performance of the catalyst. Therefore, CeO$_2$ has been widely studied in heterogeneous catalysis, and it is one of the most active catalysts among the rare-metal oxides for VOCs catalytic oxidation reactions [14,15]. Nevertheless, it is difficult to achieve complete degradation of styrene at low temperatures due to its special benzene ring and C═C bond. For instance, Li et al. [6] studied the catalytic oxidation activity of styrene with a series of Ce-substituted La$_{1-x}$Ce$_x$MnO$_3$ catalysts, and achieved completely removal below 370 ℃. In another previous study, CeO$_2$ under humid conditions was shown to achieve 100% conversion of 50 ppm styrene under thermal catalytic conditions only at 300 ℃ (T$_{90\%}$=245 ℃), and even under conditions of photothermal catalysis, T$_{90\%}$ was 226 ℃ [8]. Thus, low-temperature catalytic oxidation of styrene is still- challenging.

On the other hand, as a crucial factor for catalytic activity, the oxygen vacancy defect has been studied by many researchers in different experiments [16–18]. Deng et al. [16] concluded O$_2$ can absorb on the oxygen vacancies on the surface of defective Co$_3$O$_4$ to form reactive oxygen species, thus reducing the dissociation energy barrier of the C─H bonds. Chen et al. [19] showed that surface oxygen vacancies contribute to the catalytic activity of toluene oxidation over the α-MnO$_2$ catalyst. Zhang et al. [20] investigated the mechanism of ceria-based catalysts in hydrogenation by regulating the surface oxygen defects of CeO$_2$. Feng et al. [21] prepared four CeO$_2$ supports (rod, polyhedron, octahedron, and cubic) with different morphologies and crystal faces by the hydrothermal method, and studied their effects on the composition of the Pd species and oxygen defects on Pd/CeO$_2$ catalysts. In particular, the (110) crystal face of Pd/CeO$_2$-R with high surface oxygen mobility and lower formation energy of oxygen defects has the highest concentration of oxygen vacancies. In recent years, in addition to the concentration of oxygen vacancies, the chemical environment of lattice oxygen, including lattice distortion and site symmetry has been a research focus. Gong et al. [22] pointed that the La$_{0.5}$Ce$_{0.5}$FeO$_3$ catalyst with the greatest distortion of the FeO$_6$ octahedron exhibits excellent cycle stability, structural reversibility, and redox reversibility in the continuous CH$_4$/CO$_2$ redox cycle. Jiang et al. [13] showed that the formed Pt-O-Ce interface spontaneously distorts when a single Pt atom was stabilized by surface defect, and in turn maintained thermodynamic stability through strong metal-support interaction (SMSI). In addition, the distortion of the active interface significantly promotes the adsorption capacity of methanol and O$_2$, which is considered to be another key reason for improving the stability of SACs. However, there have been few studies on the effect of the lattice distortion on the active site in pure CeO$_2$ catalysts. Meanwhile, the control of the concentration of oxygen vacancies of CeO$_2$ through the preparation of CeO$_2$ with different morphologies, the catalytic degradation process of styrene on CeO$_2$ catalysts and the corresponding intermediate products and mechanism are still unclear and deserve further study.

Herein, four CeO$_2$ catalysts with different morphologies (sphere, rod, octahedral and cube) were prepared in this study. The relationship of the lattice distortion and oxygen vacancy concentration of the catalysts was studied through a series of characterization analyses, including the refined X-ray diffraction (XRD), Transmission electron microscopy/High resolution transmission electron microscopy (TEM/HRTEM), X-ray photoelectron spectroscopy (XPS), Raman, H$_2$-temperature-programmed reduction (H$_2$-TPR), oxygen temperature programmed desorption (O$_2$-TPD) and electron paramagnetic resonance (EPR). In addition, another goal of this work is to elucidate the role of oxygen vacancies in the catalytic styrene oxidation process, and to determine the key active sites. Moreover, the key intermediate species and the related mechanism of styrene catalytic oxidation were further analyzed by in-situ DRIFTs. ^{18}O$_2$ isotope tracing experiment further validates the involvement of oxygen species in the catalytic oxidation of styrene and DFT calculations suggest a plausible pathway for the catalytic oxidation of styrene on CeO$_2$-S (111).

2. Experimental sections

2.1. Preparation of catalysts

All chemical reagents used in this work were analytical pure and were used without further purification. CeO$_2$ catalysts with four morphologies (sphere, octahedral, rod and cube) were synthesized by the hydrothermal method according to previous studies [23] and are denoted as CeO$_2$-S, CeO$_2$-O, CeO$_2$-R and CeO$_2$-C, respectively. For the CeO$_2$-S sample, cerium-(III) nitrate hexahydrate (Ce(NO$_3$)$_3$.6H$_2$O), ethylene glycol and acetic acid were used without further purification. In addition, for other CeO$_2$ samples (octahedral, rod and cube), cerium (III) nitrate hexahydrate (Ce(NO$_3$)$_3$.6H$_2$O) and sodium hydroxide were used. All of the obtained catalysts were calcined at 500 ℃ for 2 h. For activity comparison, Pt/CeO$_2$-S catalysts were prepared by the impregnation method. The synthesis process is described in detail in the Supplementary information 1.1.

2.2. Catalytic activity tests

The catalytic performance of the synthesized catalysts was tested in a reactor. In this study, the sample (200 mg, 40–60 mesh) was stabilized by quartz cotton and placed in the middle of a quartz tube (Φ = 6.0 mm). The inlet stream was 600 ppm styrene with 25% air, and the total gas flow rate was 50 mL min^{-1} (weight space velocity (WHSV) = 15,000 mL/(g·h)). The concentration of styrene in the outlet gas was detected by gas chromatography using two flame ionization detectors and a methane converter (GC-9790II-FID, FuLi, China). The test was performed for the temperature range of 30–350 ℃ at the temperature intervals of 25 ℃. Styrene removal is defined as follows:

$$X_{styrene}(\%) = \frac{Styrene_0 - Styrene_T}{Styrene_0} \tag{1}$$

where Styrene$_0$ is the inlet concentration of styrene, and Styrene$_T$ is the outlet concentration of styrene at the reaction temperature (T).

Details of the yield, selectivity of CO$_2$, reaction rate (r$_{(styrene)}$, molC$_8$H$_8$ g^{-1} h^{-1}), the normalized initial reaction rate (r*$_{(styrene)}$, molC$_8$H$_8$ m^{-2} h^{-1}), apparent activation energies (normalized) of the oxidation reaction (E$_a$, E$_{a\text{-norm}}$, kJ mol^{-1}), and turnover frequency (TOF$_{ov}$, s^{-1}) are shown in the Supplementary information 1.4.

2.3. Catalyst characterization

Transmission electron microscopy and high-resolution transmission electron microscopy (TEM and HRTEM) images were obtained using a Tecnai G2 F30 instrument (FEI, USA) with an operating voltage of 300 kV. The X-ray powder diffraction (XRD) experiments were performed using a Bragg-Brentano-type powder diffractometer (D8 ADVANCE, Bruker, Germany), operated at 40 kV and 40 mA with Cu Kα radiation at λ = 0.15418 nm. The XRD refinements were obtained using the same equipment with the details listed in the Supplementary information 1.2 - 1.3 N$_2$ adsorption-desorption isotherms were determined at −196 ℃ using an automatic adsorption instrument (Quantachrome NOVA 4200e automated sorption analyzer, USA). Prior to the tests, the samples were degassed by nitrogen at 300 ℃ for 3 h in order to remove the physically adsorbed impurities. The BET and BJH methods were used to calculate the surface areas and the pore volumes of these catalysts.

X-ray photoelectron spectroscopy (XPS) profiles were obtained with an AXIS SUPRA (Krartas, Shimadzu) spectrometer using monochromatic

Al Kα radiation source (=1486.6 eV). The binding energy (BE) values were calibrated using the C 1 s peak at 284.8 eV. The Raman spectra were recorded under ambient conditions with a LabRAM HR800 confocal Raman spectrometer (Horiba Jobin Yvon, France) using a 325 nm laser. The electron paramagnetic resonance (EPR) measurements were carried out using an X-band A300–6/1 spectrometer (Bruker, Germany) at room temperature.

The hydrogen temperature-programmed reduction (H_2-TPR) experiments were carried out as follows: the samples (100 mg) reacted with a flow of 10 vol% H_2/Ar (30 mL min^{-1}) as the temperature increased from 100 °C to 900 °C at a heating rate of 10 °C/min. H_2 consumption was recorded using a TCD detector. The oxygen temperature-programmed desorption (O_2-TPD) experiments were carried out as follows. First, the samples (50 mg) were pretreated with He stream (30 mL min^{-1}) at 400 °C for 60 min to remove the adsorbed impurities. Then, after cooling to 50 °C, the samples were exposed to 10 vol% O_2/He flow (30 mL min^{-1}) for 1 h and then O_2/He was replaced by pure He for 1 h. Lastly, the sample was heated from 50 to 800 °C at a heating rate of 10 °C min^{-1} in He gas (30 mL min^{-1}), and the O_2 desorption was measured using the TCD detector. Styrene temperature programmed desorption (Styrene-TPD) and styrene temperature-programmed surface reaction (Styrene-TPSR) experiments were carried out using an online gas chromatograph equipped with flame ionization detectors. The characterization procedures are described in detail in the Supplementary information 1.5–1.7.

2.4. In situ DRIFTs, $^{18}O_2$ isotope tracing experiment and DFT calculations

To evaluate the adsorption and the mechanism of catalytic oxidation of styrene on the catalyst surface, in-situ diffuse reflectance infrared Fourier transform spectrometry (In-situ DRIFTs) measurements were carried out using a NicoletiS50 FT-IR spectrometer (Thermo Fisher Scientific, USA) as described in detail in the Supplementary information 1.8. In addition, the details of $^{18}O_2$ isotope tracing experiment and DFT theoretical calculations are in the Supplementary information 1.9–1.10.

3. Results and discussion

3.1. Catalysts structural properties

The morphologies and exposed lattice plane of the four samples were characterized by TEM and HRTEM with the results shown in Fig. 1. Fig. 1(a)–(d) present the TEM images of the four samples that display typical sphere, rod, octahedral and cube shapes, respectively. Fig. 1(e)–(h) exhibit the HRTEM images of the above corresponding samples. The regular lattice fringes of the samples can be observed clearly, and the main exposed lattice planes of four samples are different. As shown in Fig. 1(e)–(h), statistical analysis showed that the main exposed crystal plane of the CeO$_2$-S oxide is the (111) crystal plane, CeO$_2$-R mainly exposed (111), (100), and (110) crystal planes, CeO$_2$-O mainly exposed (110) crystal plane, and CeO$_2$-C mainly exposed (100) and (110) crystal planes. Notably, clear lattice distortion was observed for the CeO$_2$-S sample in Fig. 1(e), where the red region suggests the curving lattice fringes, and the yellow region indicates the blurred lattice fringes. It has been reported in the literature that lattice distortions such as interfacial dislocations and crystal deformations are often accompanied by oxygen vacancies [24,25].

The N_2 adsorption-desorption isotherm curves of the four CeO$_2$ samples are type IV isotherms, with H3 type hysteresis loops (Fig. S1(a)). The highest values for the specific surface area (149 m^2/g) and pore volume (0.235 cm^3/g) are observed for CeO$_2$-S. A large specific area provides a larger number of adsorption and active sites. The crystallite size and structural parameters of the samples are listed in Table 1. The results show that the crystallite sizes are in the order of CeO$_2$-S (9.6 nm), CeO$_2$-R (12.1 nm), CeO$_2$-O (13.0 nm) and CeO$_2$-C (28.5 nm). Fig. S1 shows that the samples are composed of pure cubic cerianite structure

(JCPDS No.34–0394). As shown in Fig. 2(a), the broadening of the characteristic peaks and lower diffraction peak intensity is accompanied by the shift of the (111) peak (Fig. 2(b)), indicating the existence of lattice distortion [26]. The lattice distortion of CeO$_2$ for the four different morphologies can be calculated by equation (S1) in the Supplementary information and are shown in Fig. S2. The lattice distortion values are in the order of CeO$_2$-S (0.797) > CeO$_2$-R (0.264) > CeO$_2$-O (0.056) > CeO$_2$-C (0.019). The results of the lattice distortion of the CeO$_2$ catalysts calculated based on XRD peak refinement (Fig. 2(a)) are consistent with the results obtained from the HRTEM images.

3.2. Catalytic activity for styrene oxidation

3.2.1. Styrene catalytic performance

The results for the catalytic styrene degradation performance over cerium oxides with four different morphologies are shown in Fig. 3(a). These results were obtained under the reaction condition of 600 ppm C_8H_8, 25% air and weight hourly space velocity (WHSV) of 15,000 mL/(g·h). It is observed from Fig. 3(a) that the catalytic activity curve shows a downward trend below 100 °C. This is mainly due to the adsorption of styrene over the four CeO$_2$ catalysts. As the temperature rises, the performance of adsorption decreases in the higher temperature range. With increasing temperature, the adsorption effect of the CeO$_2$ materials was converted into the catalytic activity. CeO$_2$-S exhibits the highest activity for styrene degradation among the four samples, as shown by 50% styrene degradation temperature (T_{50}) of 133 °C and 90% styrene degradation temperature (T_{90}) of 184 °C. In particularly, the T_{90} of CeO$_2$-S is much lower than those of CeO$_2$-R (219 °C), CeO$_2$-O (221 °C) and CeO$_2$-C (> 350 °C). The T_{50} and T_{90} values (the 50% and 90% C_8H_8 degradation temperature, respectively) that are used to describe the catalytic activity are listed in Table 2. The catalytic activities for styrene degradation follow the order of CeO$_2$-S > CeO$_2$-R > CeO$_2$-O > CeO$_2$-C. Compared to the reports in the literature, the catalytic oxidative degradation of styrene on the CeO$_2$-S catalyst occurs at a relatively low temperature (Table S1). Interestingly, when the activity rises to a certain level, an evident downward trend is observed for the CeO$_2$-O and CeO$_2$-C catalysts. The specific reasons for this phenomenon will be discussed later. The yield and selectivity of CO$_2$ show the same trend (CeO$_2$-S > CeO$_2$-R > CeO$_2$-O > CeO$_2$-C) with styrene catalytic activity (Fig. S3). Furthermore, Fig. S4 shows the performance of styrene catalytic oxidation and CO$_2$ yield under different WHSV conditions. More details are shown in the Supplementary information.

In general, the actual industrial VOCs emission profile contains moisture, thus 7 vol% water vapor addition is considered in the activity test. It can be seen from Fig. S5(a), although 7 vol% water vapor is introduced, there are almost no effect on the styrene degradation rate on CeO$_2$-S, CeO$_2$-R and CeO$_2$-O, except for CeO$_2$-C. This result indicate that the CeO$_2$-S sample is the ideal catalyst in industrial process. The catalytic degradation of 600 ppm styrene on 0.25% Pt/CeO$_2$-S catalyst is compared with that of CeO$_2$-S catalyst, and the result is exhibited in Fig. S5(b). It is discovered that at the low temperature (100–150 °C) stage, the 0.25% Pt/CeO$_2$-S shows the better catalytic properties than CeO$_2$-S, but the two catalysts display the similar styrene degradation performance after 150 °C. The TEM、HRTEM、STEM and H$_2$-TPR of 0.25% Pt/CeO$_2$-S is further explored in the Fig. S6. The result reveals that the addition of Pt cannot significantly improve the degradation performance of styrene, the specific reasons for this phenomenon will be studied in the further.

3.2.2. Kinetic measurements

The influence of internal and external diffusion was further excluded and the apparent activation energy was calculated, as shown in Fig. S7. The Arrhenius plots for styrene degradation < 20% are shown in Fig. 3 (b). Based on the slope obtained from the linear fitting of the Arrhenius formula, the E$_a$ values of styrene degradation were calculated for the four samples and are summarized in Table 2. The E$_{a-norm}$ value of CeO$_2$-S
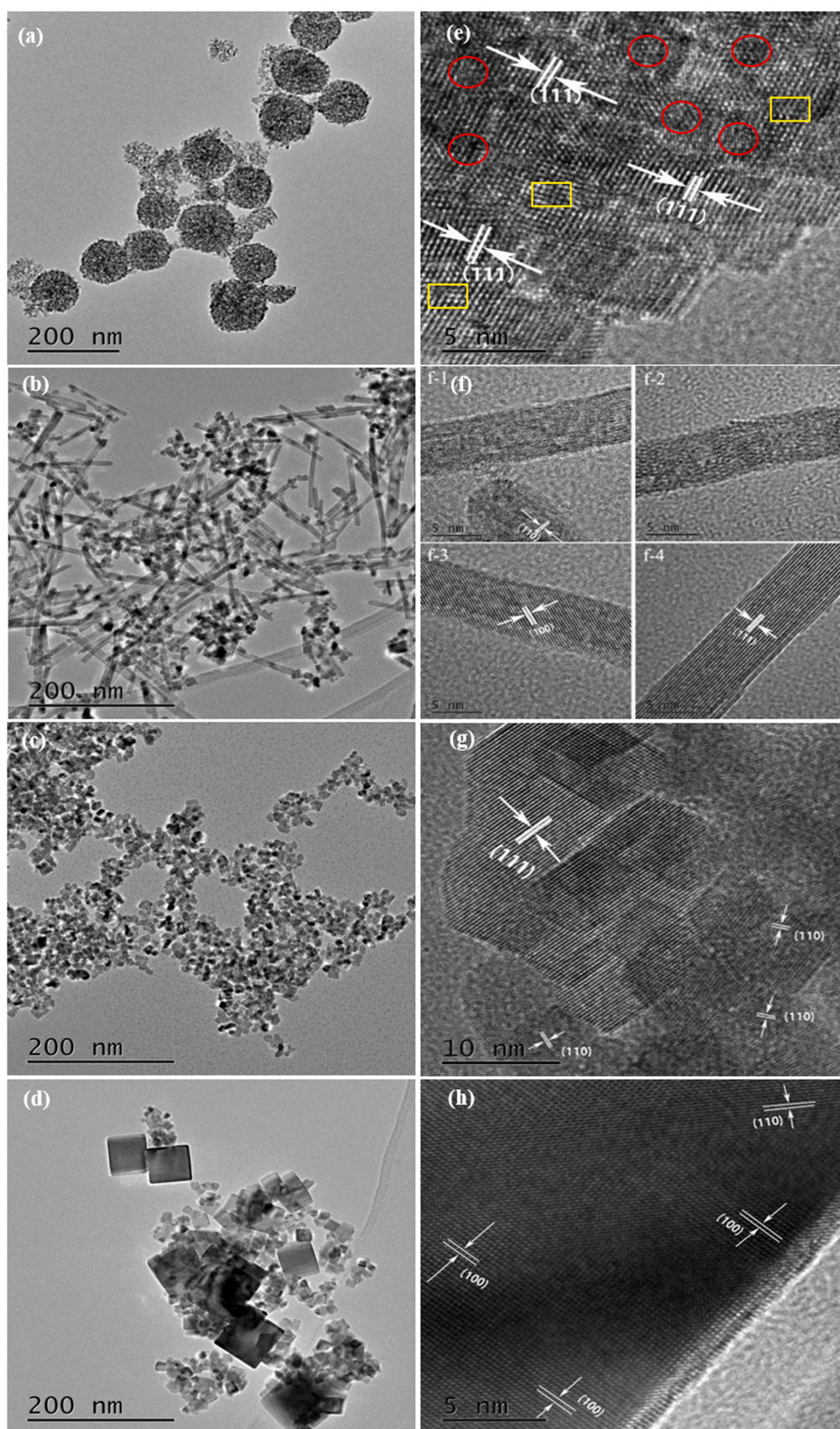
Fig. 1. TEM and corresponding HRTEM images of all the Cerium-based catalysts with different morphologies: (a), (e) CeO$_2$-S; (b), (f) CeO$_2$-R; (c), (g) CeO$_2$-O; (d), (h) CeO$_2$-C, respectively.

Table 1
The structural parameter of the samples.

Samples	STRAIN[a] (%)	FWHM of (111)	CeO_2 crystallite size (nm)[b]	CeO_2 lattice parameter (nm)	BET surface area (m^2/g)	Pore volume (cm^3/g)	BJH pore size (nm)
CeO_2-S	0.797	1.047	9.6	0.5415	148.92	0.235	5.478
CeO_2-R	0.264	0.669	12.1	0.5411	80.57	0.125	3.751
CeO_2-O	0.056	0.557	13.0	0.5416	74.89	0.153	7.556
CeO_2-C	0.019	0.381	28.5	0.5412	27.41	0.071	3.774

[a] The STRAIN means that average lattice distortion degree, calculated form S1.
[b] The crystallite size was calculated with Scherrer's formula.
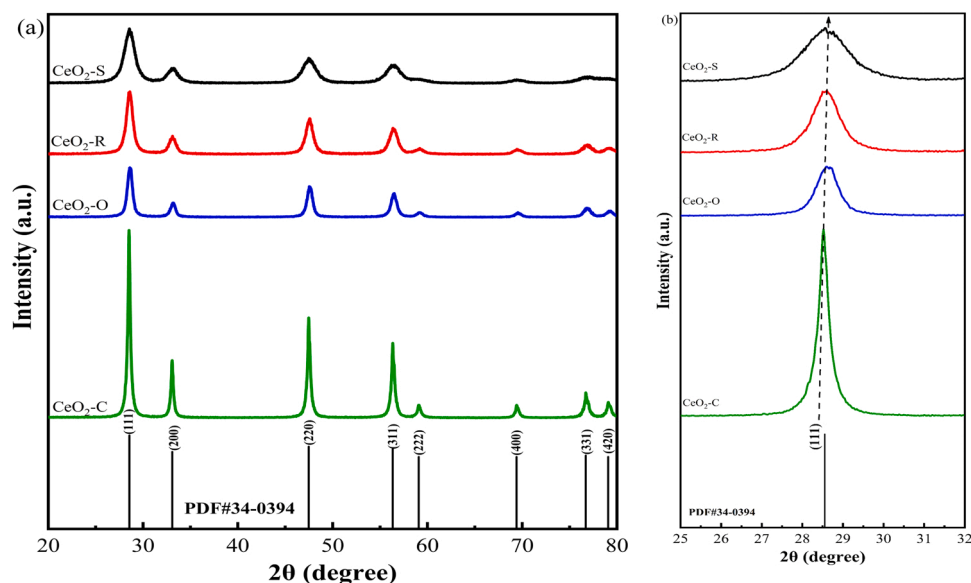
Fig. 2. (a) The retrieval of XRD pattern of cerium oxide with different morphologies (CeO_2-S, CeO_2-R, CeO_2-O and CeO_2-C); (b) The shift of (111) crystal faces (marked with dotted line) of cerium oxide with different morphologies (CeO_2-S, CeO_2-R, CeO_2-O and CeO_2-C).

is 21.79 ± 1 kJ/mol, which is lower than those of CeO_2-R (25.18 ± 1 kJ/mol), CeO_2-O (32.33 ± 2 kJ mol^{-1}) and CeO_2-C (42.70 ± 3 kJ mol^{-1}). In addition, Arrhenius plots based on the normalized reaction rates of styrene oxidation and the E_a values were also obtained. As shown in Fig. S8(a) and Table 2, the E_a values for styrene oxidation on these Ce-based catalysts are in the order of CeO_2-S< CeO_2-R < CeO_2-O < CeO_2-C, suggesting that CeO_2-S has a lower apparent activation energy. These results indicated that regardless of whether or not the specific surface area of four morphologies of CeO_2 is normalized, styrene catalytic oxidation reaction occurs more easily over CeO_2-S, followed by CeO_2-R, CeO_2-O and CeO_2-C respectively. It has been reported that the surface oxygen species are the most likely origin of the differences in E_a because surface oxygen vacancies can act as catalytic active sites that control the reaction rate [27]. The apparent activation energy was calculated without considering external mass transfer factor are shown in Fig. S8(b). It can be seen that apparent activation energy is significantly greater than considering internal and external mass transfer influences.

Furthermore, the reaction rates of different morphologies CeO_2 at 200 °C were calculated based on the relevant data obtained in the activity experiments (Fig. 3(c)). An examination of the results presented in Table 2 shows that the reaction rates are in the order of CeO_2-S> CeO_2-R > CeO_2-O > CeO_2-C, consistent with the results for the catalytic activity. The reaction rates after normalization of the specific surface area are shown in Fig. 3(d) and Table 2, which also remain consistent with the activity results. The variation of $r_{(styrene)}$ and $r^*_{(styrene)}$ for the CeO_2-S, CeO_2-R, CeO_2-O and CeO_2-C (Fig. S9(a), (b)) indicates that CeO_2-S shows a significant increase in reaction rate whether the reaction rate was normalized by S_{BET}, while CeO_2-R, CeO_2-O and CeO_2-C show

relatively slow growth trends. However, CeO_2-S and CeO_2-R show the similar $r^*_{(styrene)}$ at 175 °C. This indicates that the larger specific surface area of CeO_2-S does provide a large number of active sites for the catalytic oxidation of styrene.

Previous studies found that the formation energy of the oxygen vacancy (E_{OV}) for different crystal planes is in the order of (110) < (100) < (111) on CeO_2 catalysts [21,28]. Many studies also showed that CeO_2 catalysts with (001) and (110) crystal planes are more active than CeO_2 catalysts with (111) planes in the catalytic reaction [29,30]. Even though the main exposed crystal facets of CeO_2-S are the (111) facets (Fig. S10), CeO_2-S exhibits the highest styrene catalytic degradation activity. Therefore, the key factors that control the generation of oxygen vacancies and the active sites in the styrene catalytic oxidation process are still unclear.

3.3. Identification of active sites for styrene oxidation

3.3.1. XPS and UV-Raman analyses

The XPS spectra of Ce 3d of the four samples are shown in Figs. 4(a) and S11, and are divided into eight peaks associated with Ce 3d electrons corresponding to four pairs of spin-orbit states. The peaks were carefully assigned using CasaXPS software after the background subtraction procedure. Among the eight peaks, the Ce3d$_{5/2}$ and Ce3d$_{3/2}$ signals of the Ce^{3+} 3d final state were marked as λ' and γ', respectively. Meanwhile, the λ/λ''/λ''' and γ/γ''/γ''' peaks were assigned to the Ce3d$_{5/2}$ and Ce3d$_{3/2}$ features of the Ce^{4+} 3d species, respectively [27, 31]. It is reported that the electrons provided during the reduction of CeO_2 are usually transferred to the Ce atoms, so that Ce^{4+} is reduced to Ce^{3+}. The reduction of Ce is accompanied by the formation of oxygen
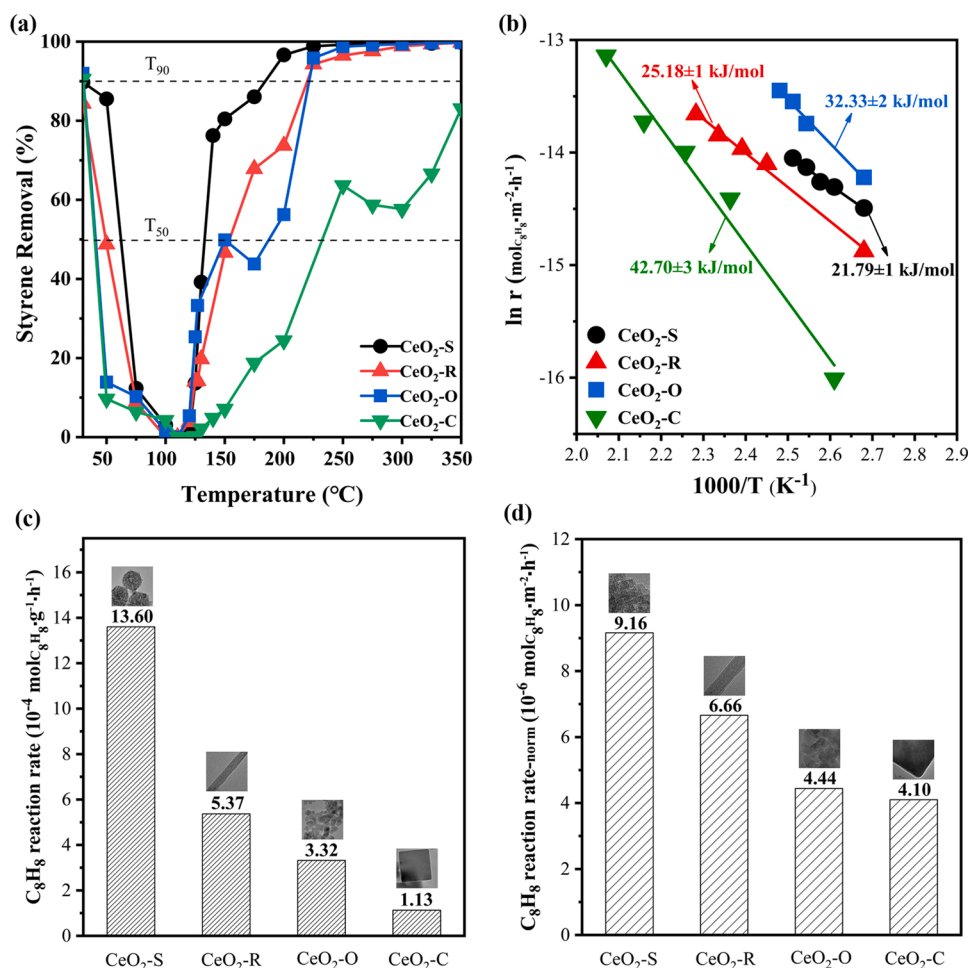
Fig. 3. (a) Styrene degradation over four different morphologies Cerium oxide (CeO_2-S, CeO_2-R, CeO_2-O, and CeO_2-C) catalysts. Reaction condition: 0.20 g catalysts, 600 ppm styrene, 25% air, total flow rate= 50 mL min^{-1}, WHSV= 15,000 mL/(g·h); (b) The S_{BET} is normalized Arrhenius plots for styrene catalytic oxidation over CeO_2-S, CeO_2-R, CeO_2-O and CeO_2-C; (c) The reaction rates ($\times 10^{-4}$ molC_8H_8 g^{-1} h^{-1}) at 200 °C for CeO_2-S, CeO_2-R, CeO_2-O and CeO_2-C; (d) The normalized reaction rates by specific surface area ($\times 10^{-6}$ molC_8H_8 m^{-2} h^{-1}) at 200 °C for CeO_2-S, CeO_2-R, CeO_2-O and CeO_2-C.

Table 2
The catalytic performance data and reaction rate (r(styrene) and r*(styrene)); E_a and E_{a-norm} over CeO_2-S, CeO_2-R, CeO_2-O, and CeO_2-C; The value of TOF_{ov} over CeO_2-S, CeO_2-R, CeO_2-O, and CeO_2-C.

Samples	T_{50} (°C)[a]	T_{90} (°C)[b]	r (styrene)[c] (200 °C)	r*(styrene)[d] (200 °C)	E_{a-norm}[e] (kJ mol^{-1})	E_{a-norm}*[f] (kJ mol^{-1})	$TOF_{OV} \times$ E-06 at 125 °C (s^{-1})
CeO_2-S	133	184	13.60E-04	9.16E-06	21.79 ± 1	102.19	6.46
CeO_2-R	153	219	5.37E-04	6.66E-06	25.18 ± 1	112.43	3.08
CeO_2-O	151	221	3.32E-04	4.44E-06	32.33 ± 2	119.45	2.42
CeO_2-C	232	> 350	1.13E-04	4.10E-06	42.70 ± 3	137.28	0.63

[a] T_{50} means the reaction temperature corresponding to the toluene catalytic combustion conversion of 50%.
[b] T_{90} means the reaction temperature corresponding to the toluene catalytic combustion conversion of 90%.
[c] Calculated from reaction equation (S5).
[d] Calculated from reaction equation (S6).
[e] Ea-norm means that the apparent activation energy normalized by specific surface area according to the Arrhenius formula.
[f] Ea-norm* means that the apparent activation energy normalized by specific surface area (The external diffusion factor is not excluded) according to the Arrhenius formula.

vacancies (OVs) and appearance of unsaturated chemical bonds that can generate more strongly chemically adsorbed oxygen species to promote the catalytic oxidation reaction [8]. The amounts of Ce^{3+} relative to the total number of Ce atom in CeO_2-S, CeO_2-R, CeO_2-O and CeO_2-C are 26.08%, 25.25%, 21.12% and 20.53%, respectively (Table 2). These results mean that CeO_2-S has the highest concentration of surface oxygen vacancies. Fig. 4(b) shows the O1s spectra that were divided into four peaks. The four peaks are assigned to lattice oxygen (O_{latt}, O^{2-}) at 529.2 eV [8,32], surface and adsorbed oxygen species (O_{ads}, O_2^- or O_2^{2-}) at 529.8 eV and 531.8 eV, respectively, and surface hydroxyl oxygen (O_{adsO-H}) at 533.3 eV [33]. The O_{ads}/ ($O_{latt} + O_{ads} + O_{adsO-H}$) ratio can be

used to explain the concentration of surface adsorbed oxygen, and provides a further measure of the concentration of surface oxygen vacancies [10,32]. As listed in Table 3, CeO_2-S possesses the highest proportion of adsorbed oxygen species. According to the Ce 3d and O 1 s XPS results, the concentration of surface oxygen vacancies was found to be in the order of CeO_2-C< CeO_2-O < CeO_2-R< CeO_2-S.

The UV-Raman spectra of the four different morphologies of CeO_2 are displayed in Figs. 4(c) and S12. The strong peak at 455 cm^{-1} is assigned to the F_{2g} mode of the fluorite-type CeO_2 structure that is due to the symmetrical stretching vibration of the O^{2-} surrounding the Ce^{4+} [27]. Another weak and broad peak at 600 cm^{-1} is attributed to the
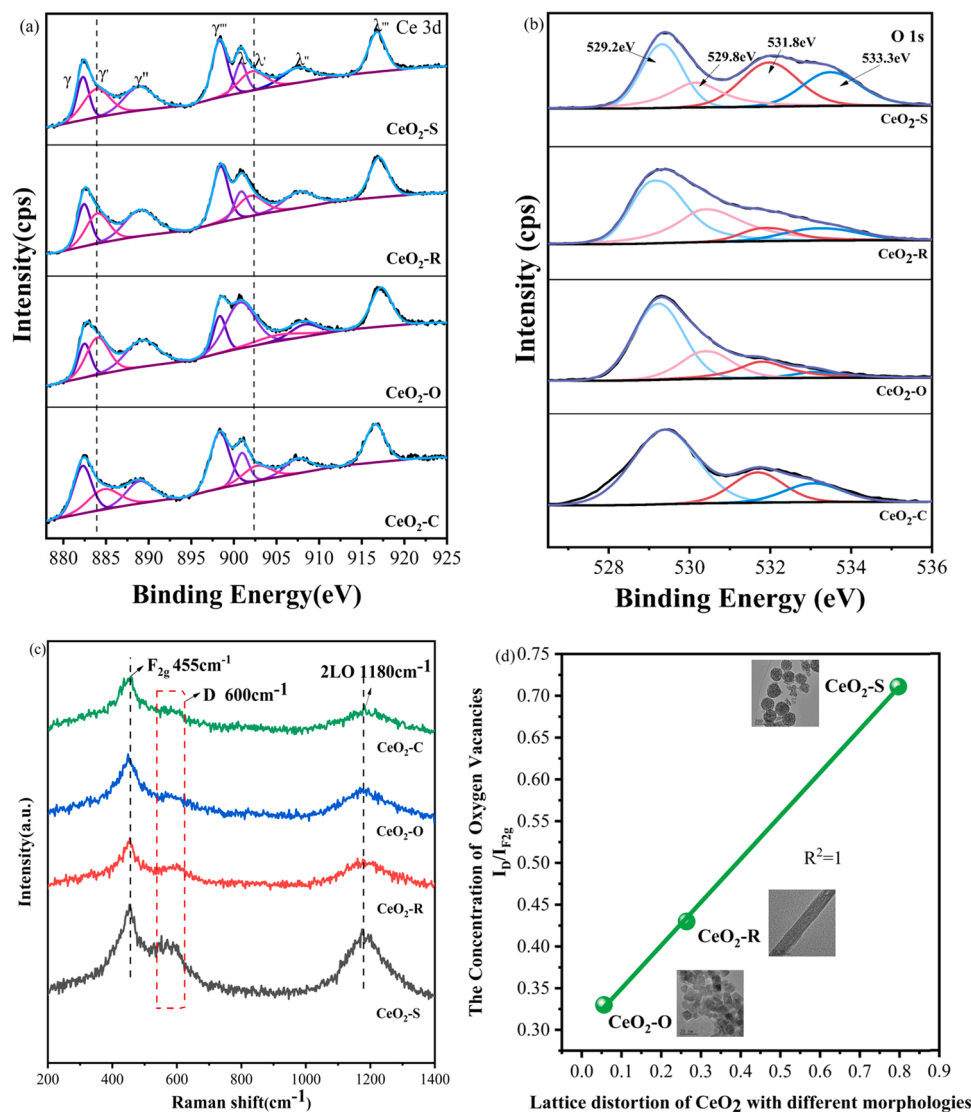
Fig. 4. XPS spectra and UV-Raman spectra of fresh CeO₂-S, CeO₂-R, CeO₂-O and CeO₂-C samples. (a) Ce 3d XPS spectra of samples; (b) O 1s XPS spectra of samples; (c) UV Raman patterns of samples; (d) Correlation of the lattice distortion of CeO₂ with different morphologies (CeO₂-S, CeO₂-R and CeO₂-O) with Oxygen vacancies concentration (The ratio of I_D/I_{F2g} represents the oxygen vacancy concentration).

Table 3
Ce 3d and O 1s XPS data and Raman data of CeO₂-S, CeO₂-R, CeO₂-O, and CeO₂-C.

Samples	$Ce^{3+}/(Ce^{3+}+Ce^{4+})$	$O_{ads}/(O_{latt}+O_{ads}+O_{adsO-H})$	I_D/I_{F2g} [a]
CeO₂-S	26.08%	47.53%	0.711
CeO₂-R	25.25%	42.34%	0.430
CeO₂-O	21.12%	34.91%	0.330
CeO₂-C	20.53%	13.81%	0.199

[a] The I_D/I_{F2g} are calculated from the ratio of the peak area 600 cm⁻¹ /455 cm⁻¹ from UV-Raman spectrum.

band of the defect-induced (D) mode that is the characteristic peak of the oxygen vacancies arising due to the presence of Ce^{3+} [34]. The last peak at 1180 cm⁻¹ can be attributed to the second-order longitudinal optical (2LO) mode [32]. The values of I_D/I_{F2g} represent the relative concentration of oxygen vacancy [35] and are listed in Table 3. The value of I_D/I_{F2g} over four samples was in the order of CeO₂-S> CeO₂-R> CeO₂-O> CeO₂-C, which is consistent with the XPS results. The specific fitting diagrams of correlation analysis between the Raman and XPS results are shown in Fig. S13. These results directly

indicate that there is positive correlation between the oxygen vacancy concentration and Ce^{3+} content, as well as between oxygen vacancy concentration and adsorbed oxygen content. TOF_{ov} represents that the number of styrene reactions at each active site per unit time based on oxygen vacancy concentration of CeO₂, the amount of oxygen vacancies is evaluated based on the $Ce^{3+}/(Ce^{3+}+Ce^{4+})$ of the XPS spectra (Fig. 4 (b)). Fig. S14(a) shows that the TOF_{ov} value at 125 °C for CeO₂-S, CeO₂-R, CeO₂-O and CeO₂-C were 6.46×10^{-6}, 3.08×10^{-6}, 2.42×10^{-6}, and 0.63×10^{-6} s⁻¹, respectively. Furthermore, Fig. S14 (b) shows that the TOF_{ov} values over CeO₂ increase with increasing temperature, and the TOF_{ov} valve for CeO₂-S is much greater than those for CeO₂-R, CeO₂-O and CeO₂-C. Thus, oxygen vacancies play an important role in controlling the rate of styrene catalytic oxidation from the results of XPS, Raman and TOF_{ov} values.

The correlation between the lattice distortion of CeO₂ with different morphologies and concentration of oxygen vacancies is shown in Fig. 4 (d) (Fig. S15). The results show that lattice distortion and oxygen concentration are linearly correlated, suggesting that the greater degree of lattice distortion favors the generation of a large number of oxygen vacancies. The highest I_D/I_{F2g} value is obtained for the CeO₂-S sample, revealing that the increased CeO₂ catalyst lattice distortion will strongly

promote the concentration of oxygen vacancies. In summary, the reaction process of CeO_2 obtained by solvothermal and hydrothermal methods is different. It is worth noting that the CeO_2-S is prepared by solvothermal method. Through the observation of HRTEM images of CeO_2 catalysts, it was found that there were many curving and blurred lattice fringes on CeO_2-S. This revealed the surface of the CeO_2-S were rougher than the others, indicating surface reconstruction, which caused by the lattice distortion, occurred on CeO_2-S. Thus, the lattice distortion is the key factor to form oxygen vacancies on CeO_2 catalysts with four different morphologies.

3.3.2. Redox properties of the catalysts

The reduction capacity and the activity of surface and lattice oxygen of CeO_2 with different morphologies was characterized via temperature-programmed reduction (H_2-TPR) measurements. Two obvious reduction peaks are observed in Fig. 5(a) that reflect the activity of oxygen species on CeO_2 catalysts. The first peak (low- temperature peak, <600 ℃) represents the reduction of surface oxygen (O_2^- and O^-). The second reduction peak can be assigned to the reduction of lattice oxygen species (O^{2-}, >600 ℃) [35,36]. For the low-temperature peak, the order of peak intensities is CeO_2-S > CeO_2-R >CeO_2-O > CeO_2-C. These results mean that the H_2 consumption of CeO_2-S is much greater than those of the other three samples, indicating that the CeO_2-S sample contains more surface oxygen species. Compared to CeO_2-R (472 ℃), CeO_2-O (477 ℃) and CeO_2-C (488 ℃), an evident decrease in the reduction temperature was observed for CeO_2-S (441 ℃). Therefore, CeO_2-S not only has abundant surface oxygen species, but also surface oxygen species are more active and more easily reduced.

The results of the temperature programmed desorption of oxygen (O_2-TPD) measurements for the CeO_2 catalysts are shown in Fig. 5(b). The first desorption peak is found at 150 ℃ and can be assigned to the release of physisorbed oxygen (O_2) and chemisorbed oxygen species (O_2^- or O_2^{2-}) in the vicinity of the oxygen vacancies [9]. Meanwhile, the intensities of the peaks for chemisorbed oxygen are in the order of CeO_2-S > CeO_2-R > CeO_2-O. These results reveal that CeO_2-S has a higher oxygen vacancy content that enables it to produce the largest amount of surface adsorbed oxygen species, which is consistent with the activity results. The H_2-TPR and O_2-TPD results further indicate that surface-adsorbed oxygen species that are produced by oxygen vacancies play an important role in the styrene degradation reaction process.

3.3.3. Correlation of oxygen vacancies with styrene oxidation activity

It is believed that a greater concentration of oxygen vacancies is accompanied by the formation of more Ce^{3+} species, leading to charge imbalance and unsaturated chemical bonds, and generating more strongly chemisorbed oxygen species to improve the styrene catalytic oxidation performance [15,37]. To further identify the key active site and its role in styrene degradation on the four CeO_2 catalysts with different morphologies, correlation analysis between various factors was carried out. As shown in Fig. 6(a) and (b), the amount of physisorbed and chemisorbed oxygen species showed a clear linear relationship with the concentration of oxygen vacancies. These results demonstrate the key roles of OVs in the adsorption and activation of O_2 [38]. Fig. 6(c) and (d) show the correlation of the fitted area of the surface oxygen species for H_2-TPR and O_2-TPD with the oxidation rate of styrene at 200 ℃. It is observed that the oxidation rate of styrene exhibited a linear increase with increasing amount of surface oxygen species, indicating that the adsorbed oxygen species have an important effect on the reaction rate of styrene oxidation. These results suggest that oxygen vacancies of CeO_2 can adsorb and activate oxygen molecules to form active oxygen species and further indicate that the adsorbed oxygen species are responsible for styrene oxidation activity.

3.4. Mechanism analysis of styrene oxidation

3.4.1. Identification of the role of oxygen vacancies in styrene degradation

Fig. 7(a) shows the styrene desorption peaks of all samples in the range of 90–115 ℃. The desorption temperatures of CeO_2-S, CeO_2-R, CeO_2-O and CeO_2-C are observed to be 111.8, 102.7, 100.6 and 85.2 ℃, respectively. Thus, the desorption temperature of styrene on CeO_2-S catalyst is the highest, demonstrating that styrene binds more strongly to CeO_2-S. Furthermore, Fig. 7(a) shows that the area of the desorption peak is in the order of CeO_2-S> CeO_2-R> CeO_2-O> CeO_2-C. This indicates that CeO_2-S has the strongest adsorption capacity for styrene.

The Styrene-TPSR profiles of the CeO_2 samples are presented in Fig. 7 (b). The results show that surface adsorbed oxygen species oxidize some of the styrene to CO_2. For CeO_2-S, a large broad desorption peak of styrene before 180 ℃ is observed that is classified as strongly physisorbed styrene. Accompanied by desorbed styrene, a stronger peak of CO_2 appeared at 90 ℃. The subsequent broad peaks of CO_2 at 310 ℃ and 430 ℃ were attributed to the oxidation of the chemisorbed styrene. These results indicate that CeO_2-S shows the highest styrene adsorption capacity (Fig. 7(a)) and CO_2 production (Fig. S16). Moreover, the temperature of the CO_2 formation peaks for CeO_2-S (90 ℃) is lower than those for CeO_2-R (93 ℃), CeO_2-O (95 ℃) and CeO_2-C (165 ℃). This demonstrates that the CeO_2-S are rich in oxygen vacancies, thus generating more reactive oxygen species (surface adsorbed oxygen) and promoting the styrene oxidation. Particularly, due to the N_2 was
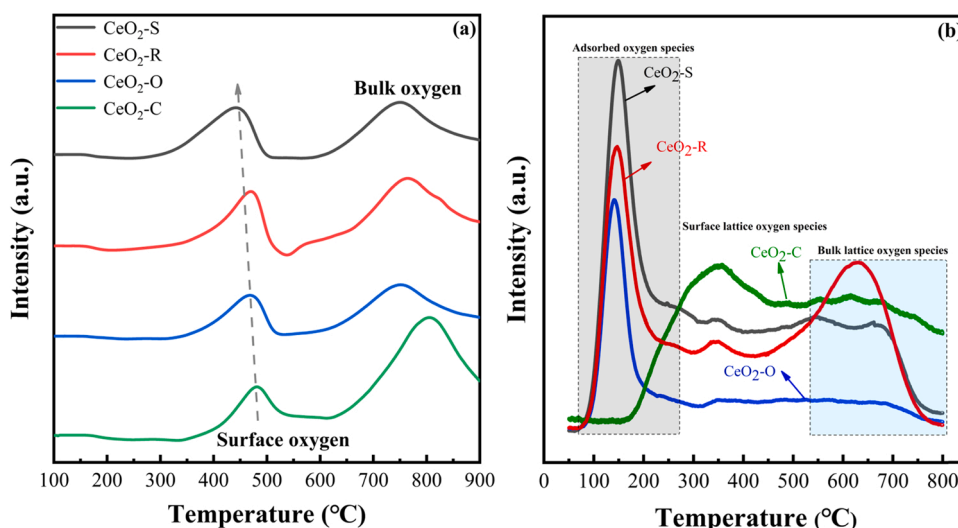

Fig. 5. (a) H_2-TPR and (b) O_2-TPD profiles of CeO_2-S, CeO_2-R, CeO_2-O, and CeO_2-C catalysts, respectively.
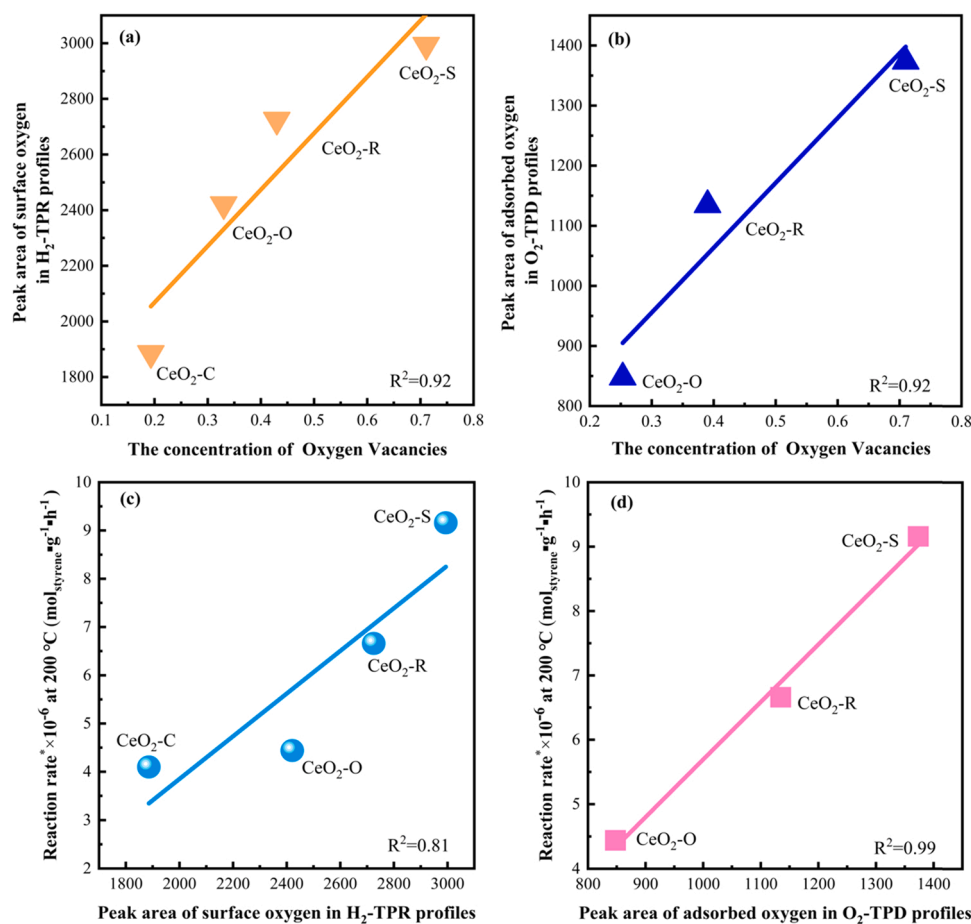
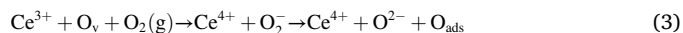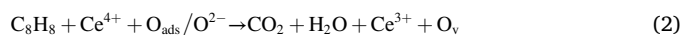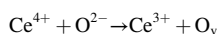**Fig. 6.** Correlation analysis. (a) Correlation of fitted area of H_2-TPR with Oxygen vacancies concentration. (b) Correlation of fitted area of O_2-TPD with Oxygen vacancies concentration (I_D/I_{F2g} means the Oxygen vacancies concentration). (c) Correlation of the fitted area of surface oxygen species with normalized oxidation rate of styrene (at 200 °C), H_2-TPR. (d) Correlation of the fitted area of adsorbed oxygen species with normalized oxidation rate of styrene (at 200 °C), O_2-TPD.

continuously introduced during the temperature program, this means that in the absence of gas-phase oxygen, once the surface adsorbed oxygen has been consumed, the adsorbed-activated styrene will be oxidized by the lattice oxygen migrated from the bulk ceria. CeO_2-S not only has abundant surface adsorbed oxygen, but also has a stronger capability of lattice oxygen migration than CeO_2-S, CeO_2-R and CeO_2-C due to abundant oxygen vacancies. Thus, the adsorption and activation of styrene with oxygen vacancies is the controlling step in styrene oxidation on CeO_2 catalysts with different morphologies. These above phenomena are in accordance with the well-known Sabatier principle that a suitable molecule-surface interaction is beneficial for the subsequent reaction of the molecule [39].

The used CeO_2 catalysts were characterized by XPS (Fig. S17) and the molar ratios of the various Ce (Fig. 7(c)) and O (Fig. 7(d)) are summarized in Table S2. It is clearly that the contents of Ce^{3+} and surface adsorbed oxygen are significantly reduced after the reaction for the four CeO_2 catalysts. It can be preliminarily inferred that Ce^{3+} and surface adsorbed oxygen on the CeO_2 surface participate in the reaction process of styrene catalytic oxidation. It is further demonstrated that the surface adsorbed oxygen species produced on oxygen vacancies are the key active sites in the styrene catalytic oxidation. The main reason for the decrease in Ce^{3+} content (oxygen vacancies concentration) is that both gas-phase oxygen and lattice oxygen are rapidly activated and fill into the oxygen vacancies quickly. The following two steps further illustrate how Ce^{3+} and surface adsorbed oxygen species participate in the reaction:

$$Ce^{4+} + O^{2-} \rightarrow Ce^{3+} + O_v$$

$$C_8H_8 + Ce^{4+} + O_{ads}/O^{2-} \rightarrow CO_2 + H_2O + Ce^{3+} + O_v \quad (2)$$

$$Ce^{3+} + O_v + O_2(g) \rightarrow Ce^{4+} + O_2^- \rightarrow Ce^{4+} + O^{2-} + O_{ads} \quad (3)$$

In addition, EPR characterization was performed with the results shown in Fig. S18(a). The peak intensity of CeO_2-S at g= 1.96 changes significantly after styrene adsorption, indicating that Ce^{3+} concentration decreases, and suggesting a decrease in the amount of oxygen vacancies. Furthermore, I_D/I_{F2g} of UV-Raman spectra was significantly reduced after styrene adsorption (Fig. S18(b)). The NH_3-TPD characterization results are shown in Fig. S18(c). Due to the difference between the electronegativity of the Ce and O atoms, the introduction of OV_S will cause a substantial increase in the acid sites on the catalyst surface [8]. Fig. S18(c), (d) shows that the CeO_2-S exhibits the maximum amount of Lewis acid sites, indicating its greater oxygen vacancy content [8]. Additionally, abundant Brønsted acid sites promote the molecular adsorption of VOC, accelerate the regeneration of hydroxyl groups on the surface, and facilitates the decomposition of intermediates in the VOC oxidation process [13]. Therefore, the results of EPR, UV-Raman, Styrene-TPD and Styrene-TPSR reveal that the oxygen vacancies can not only adsorb and activate gas-phase oxygen to increase the mobility and activity of oxygen species, but can also activate styrene by adsorption.

3.4.2. Styrene oxidation process studies

The in-situ DRIFTS technique was used to elucidate the reaction process and the key intermediates of the styrene adsorption-oxidation process on the CeO_2-S, CeO_2-R, CeO_2-O and CeO_2-C catalysts. The
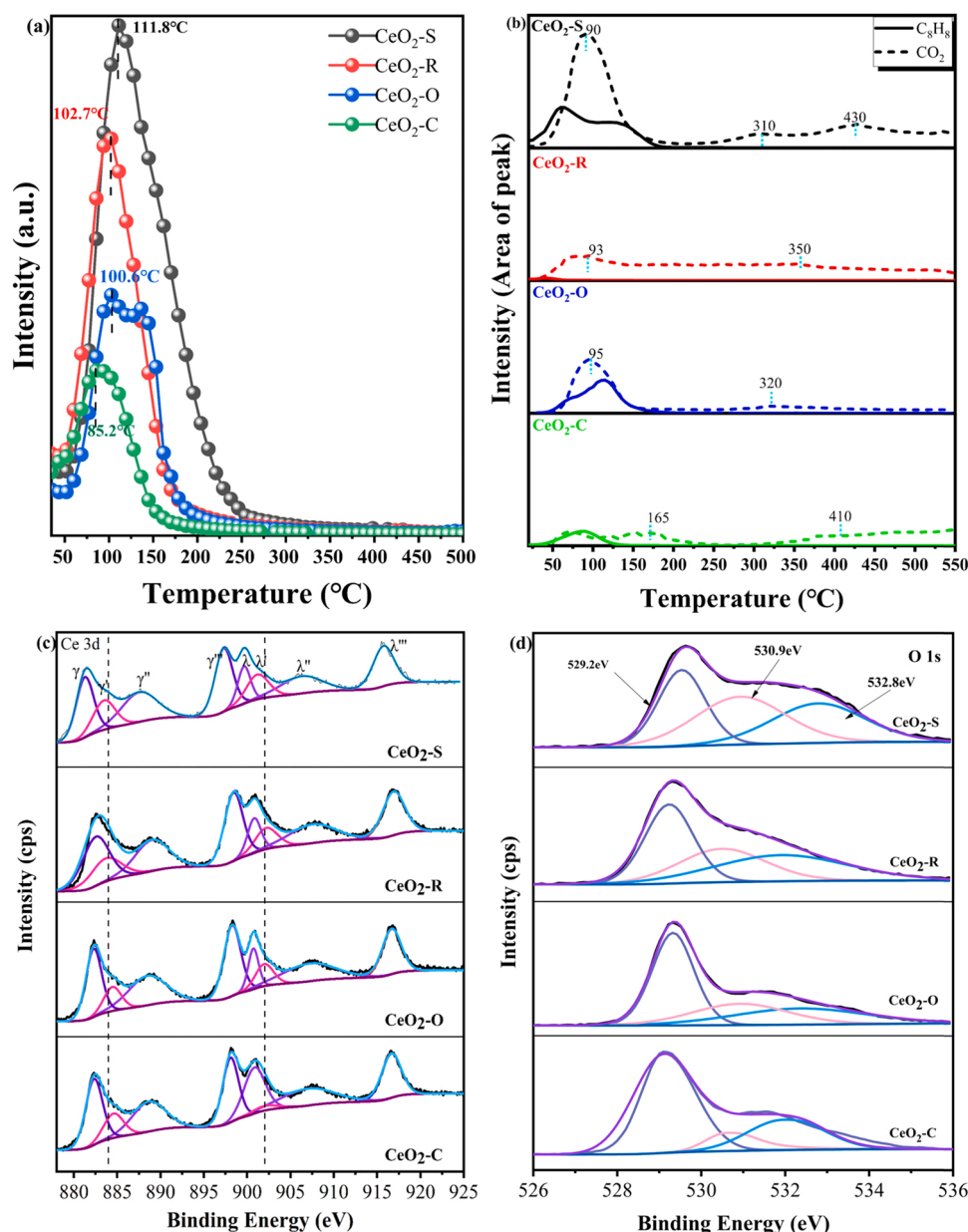
Fig. 7. (a) Styrene-TPD profiles of CeO$_2$-S, CeO$_2$-R, CeO$_2$-O, and CeO$_2$-C catalysts; (b) Styrene-TPSR profiles of CeO$_2$-S, CeO$_2$-R, CeO$_2$-O, and CeO$_2$-C catalysts, respectively; XPS spectra of (c) Ce 3d, and (d) O 1s for the used CeO$_2$-S, CeO$_2$-R, CeO$_2$-O and CeO$_2$-C catalysts on the surfaces of Ce-based catalysts.

information about various intermediates involved in the catalysis on the CeO$_2$ surface is summarized in Table S3 as well as the text commentary that follows. As shown in Fig. 8, with increasing temperature and time, the surface adsorbed species of the CeO$_2$ catalysts with different morphologies showed the different changes.

Fig. 8(a) (Fig. S19(a)) shows a typical set of temperature-dependent DRIFTS spectra during styrene oxidation process over the best-performing CeO$_2$-S catalyst in the temperature range of 30–350 °C. When 400 ppm styrene/Air was introduced into the reaction system, some weak bands appearing at 3100–3100, 1653, 1499, 1449, 1410–1390 cm^{-1} are immediately observed at 30 °C, indicating that styrene is mainly adsorbed on the surface of the CeO$_2$ catalyst at low temperature [40,41], and no obvious oxidation reaction occurs at this time. As the temperature rises to 75 °C, the characteristic peaks of styrene gradually weakened and then disappeared at 125 °C, and some clear peaks can be observed in the 1800–1000 cm^{-1} range along with the hydrogen bonded-OH groups [42,43]. This is consistent with the result of the catalytic activity experiments. The bands at 1180, 1150,

1099, 1056 cm^{-1} (υ(C-O)) and 3700 cm^{-1} (hydroxyl) appear with increasing temperature, indicating that the adsorbed styrene can be transformed into benzyl alcohol by breaking the C=C double bond of the vinyl groups. When the temperature is above 150 °C, the bands located at approximately 2820, 2723 cm^{-1} (υ(C-H)), and 1743 cm^{-1} (υ_s(C=O)) could be assigned to the formation of aldehydic species [44, 45]. Meanwhile, the bands at 1546 and 1368 cm^{-1} for the asymmetric and symmetric stretching vibrations of carboxylates (-COO$^-$) appeared [46], corresponding to carboxylate groups and suggesting the formation of benzoate species (C$_6$H$_5$-COO$^-$). Benzoate species are considered to be an important intermediate in the styrene catalytic oxidation process. In addition, the relative position of the asymmetric (1546 cm^{-1}) and symmetric (1368 cm^{-1}) stretching vibrations about carboxylate (-COO$^-$) groups very close to the Δ_υ value for the ion of approximately 178 cm^{-1}, suggesting that the carboxylate species with a bridging structure are coupled with Ce ions on the surface of the cerium-based catalysts. This result indicates that the adsorbed styrene can interact with the oxygen species on the catalyst surface [47]. As shown in Fig. 8(a), various
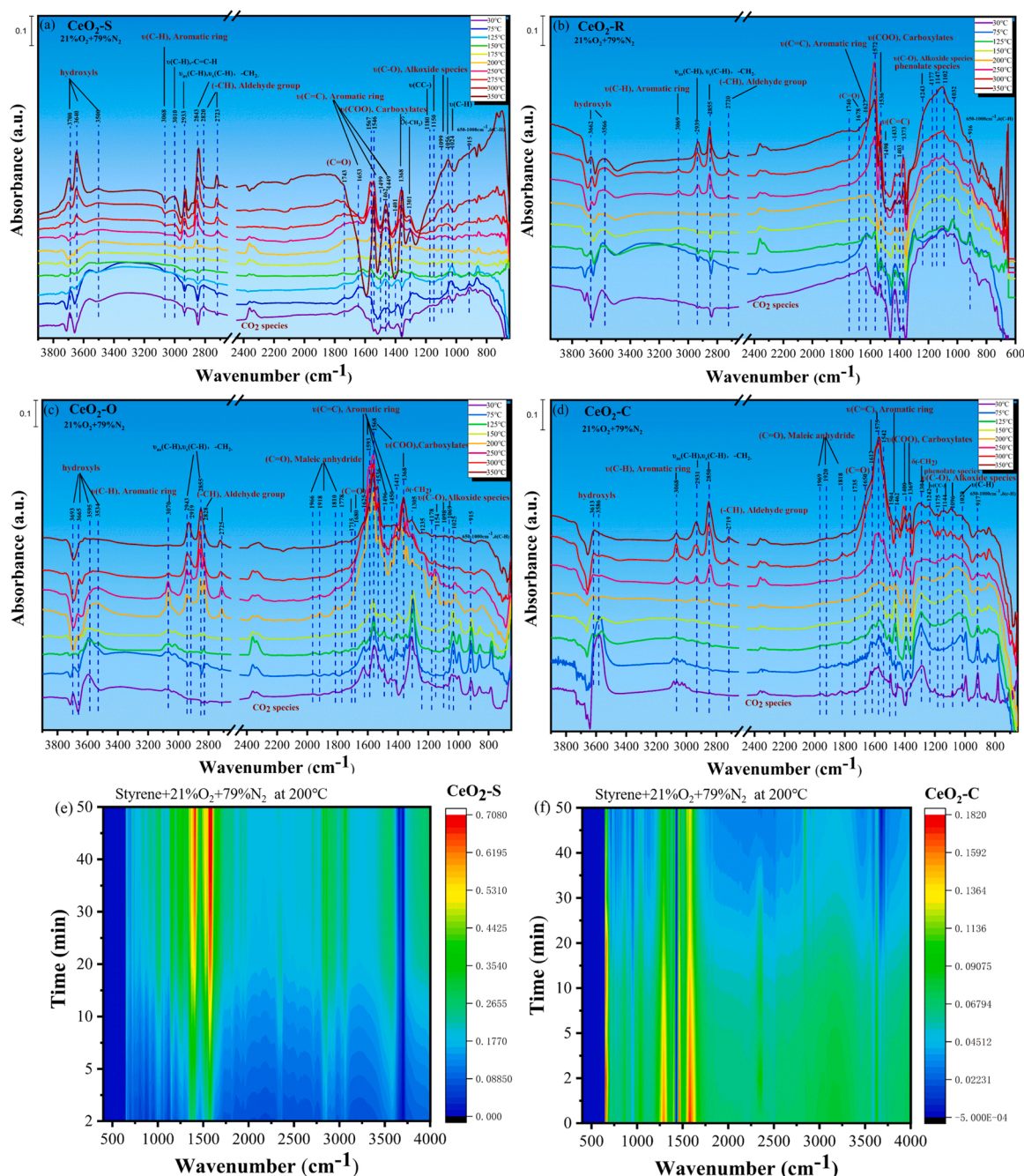
Fig. 8. In-situ DRIFTS of styrene oxidation over (a) CeO2-S; (b) CeO2-R; (c) CeO2-O; (d) CeO2-C under series of temperature (reaction condition: 400 ppm styrene + balance synthetic air with a total flow rate of 128 mL min^{-1}). In-situ DRIFTS of styrene oxidation corresponding mapping results over (e) CeO2-S and (f) CeO2-C within 50 min at 200 °C (Reaction condition: 400 ppm styrene + balance synthetic air with a total flow rate of 128 mL min^{-1}).

intermediates were gradually accumulated on the catalysts surface and reached the maximum amount with the temperature increase to 350 °C, with the bands for the -OH groups (3200–3700 cm^{-1}), alkoxide species (1099, 1056 cm^{-1}) [25,48], and benzaldehyde species (2820, 2723 and 1743 cm^{-1}) increasing in intensity. By contrast, the adsorption band at 1401 cm^{-1} attributed to carbonate species [49] disappeared above 250 °C. These results also indicate that carbonate species are important intermediates for the catalytic oxidation of styrene that can be preferentially oxidized to CO_2 and H_2O on the catalyst surface at high temperature [48].

As shown in Figs. 8(b) and S19(b), the bands at 1433, 1498, 1572 and 1627 cm^{-1} are related to the typical aromatic ring vibration bands. This indicates that styrene is also mainly adsorbed on the surface of

CeO2-R catalyst at low temperature. Four characteristic peaks gradually disappear with increasing temperature, and new characteristic peaks appear, indicating that styrene was oxidized on the catalyst surface. Similar with the CeO2-S, the main intermediates of alcohol species, aldehyde species and carboxylate species gradually appear as the temperature increases. However, the clear new bands at 2855 and 2720 cm^{-1} assigned to C-H stretching vibration of aldehyde groups [25] begin to appear at 200 °C. At 350 °C, more intermediate products of benzyl alcohol species (1200–1000 cm^{-1}) and phenolate species (1243 cm^{-1}) are formed, and the intensity of the peak for benzoate species (1536 and 1373 cm^{-1}) decrease. This is mainly because that CeO2-R has fewer oxygen vacancies than CeO2-S, which leads to a lack of adsorbed oxygen and a weaker mobility of lattice oxygen, resulting in

not further oxidation of benzyl alcohol species and phenolates. These results suggest that the styrene catalytic oxidation rate on CeO$_2$-R is lower than that on CeO$_2$-S.

Fig. 8(c), (d) shows a set of typical temperature-dependent DRIFTS spectra during the styrene oxidation process on the CeO$_2$-O and CeO$_2$-C catalysts in the temperature range of 30–350 ℃. Different from CeO$_2$-S and CeO$_2$-R, CeO$_2$-O and CeO$_2$-C show some more obvious weak bands belonging to maleic anhydride (1966, 1918, 1810 and 1778 cm^{-1}) [50]. Moreover, two small but clear bands at 1715 and 1680 cm^{-1} are observed in the DRIFTS spectra of CeO$_2$-O and CeO$_2$-C in the temperature range of 75–250 ℃ (Fig. S19(c), (d)) that may be due to the formation of benzoquinone species [50], while these two bands are almost invisible in the DRIFTS spectra of CeO$_2$-S and CeO$_2$-R. It is speculated that the reaction rates for CeO$_2$-S and CeO$_2$-R are higher than those for CeO$_2$-O and CeO$_2$-C due to the higher number of oxygen vacancies, leading to the rapid decomposition of the benzoquinone species into CO$_2$ and H$_2$O as final products. A band at approximately 915 cm^{-1} is also observed (Fig. 8(a)–(d)), indicating the formation of the saturated cyclic five-membered anhydride species [51]. Those species are the important intermediates in the process of aromatic ring cleavage, suggesting the effective facilitation of the deep oxidation of styrene in the ring-opening [52]. Combined with the analysis of the catalytic activity, these results show that CeO$_2$-O displays a decrease in the styrene degradation rate after 150 ℃ due to the accumulation of maleic anhydride species. In addition, the same phenomenon is also found for the CeO$_2$-C catalyst at temperatures higher than 250 ℃. Furthermore, for the CeO$_2$-O, the intensities of the different bands attributed to alcohol species (1069, 1098, 1154 and 1178 cm^{-1}) first increase and then gradually decrease from 75 to 350 ℃. When the temperature reaches 125 ℃, the intensities corresponding to the aldehyde species (2826, 2711 and 1778 cm^{-1}) and carboxylate species (1555, 1365 cm^{-1}) increase with the temperature, and then gradually decrease after 250 ℃. For CeO$_2$-C, a minimal amount of hydroxyl groups is generated in the range of 35–350 ℃, and alcohol species (1096, 1144 and 1175 cm^{-1}), aldehyde species (2850, 2719 and 1650 cm^{-1}) and carboxylate species (1541 and 1369 cm^{-1}) gradually accumulate after 250 ℃. Furthermore, carboxylates (1546 cm^{-1} and 1368 cm^{-1}) are the pivotal intermediates before and after the opening of the aromatic ring. For CeO$_2$-S, the formation of benzoate species is significantly more than that of CeO$_2$-R, CeO$_2$-O and CeO$_2$-C, which appeared at 150 ℃, significantly lower than CeO$_2$-R (200 ℃), CeO$_2$-O (200 ℃) and CeO$_2$-C (250 ℃). These results indicate that the deep oxidation ability of CeO$_2$-S is better than CeO$_2$-R, CeO$_2$-O and CeO$_2$-C. In summary, these observations reveal that the oxidation of styrene molecules on CeO$_2$-S, CeO$_2$-R, CeO$_2$-O and CeO$_2$-C may proceed through similar reaction processes. But because of the different concentration of oxygen vacancies, the rates of catalytic oxidation of styrene on four morphologies of CeO$_2$ are different.

Comparing the DRIFTS spectra of the four different morphologies of CeO$_2$ for the change of the band at 915 cm^{-1}, it is observed that the aromatic ring of styrene can be broken at room temperature. It is important to note that for the CeO$_2$-S catalyst, more adsorption bands corresponding to hydroxyl and adsorbed water (3700, 3640 and 3500 cm^{-1}) can be detected. This is because the higher activity of the CeO$_2$-S catalyst leads to enhanced production of -OH groups and water molecules [53]. The DRIFTS results are consistent with the results for the catalytic activity of the four catalysts.

Fig. 8(e), (f) (Fig. S19(e), (f)) show in-situ DRIFTS of styrene oxidation on CeO$_2$-S and CeO$_2$-C at 200 ℃ within 50 min. The benzyl alcohol species (2942, 2929, 2854, 1151, and 1069 cm^{-1}), benzaldehyde species (2834, 2736, 2715 and 1649 cm^{-1}), benzoate species (1538, 1403 cm^{-1}), phenol (1238 cm^{-1}) and maleic anhydride species (1960, 1920 and 1815 cm^{-1}) can be observed in the DRIFTS spectra for CeO$_2$-S and CeO$_2$-C (part of intermediates are less or invisible), and these species accumulated on the catalyst surface with longer time. However, unlike CeO$_2$-S, CeO$_2$-C only shows the accumulation of benzaldehyde (2842, 2722 and 1744 cm^{-1}) over the time, while the peaks for the other

intermediates remain unchanged, suggesting that benzaldehyde species are the main chemical adsorption species on CeO$_2$-C. In addition, less of the final CO$_2$ product is generated on CeO$_2$-C. Not only that, significantly more benzoate species (1578 cm^{-1}) and acetates (1403 cm^{-1}) were produced on the CeO$_2$-S than CeO$_2$-C, both of which are important intermediates before and after ring opening of the benzene ring. These results also indicate that styrene can be oxidized faster and to greater extent on the CeO$_2$-S. Due to the abundant oxygen vacancies the deep oxidation process of styrene can occur on CeO$_2$-S.

In the process, the breaking of the C═C bond may be the rate determining step for the styrene catalytic oxidation. The possible adsorption and oxidation mechanisms of styrene on CeO$_2$-S are summarized in Scheme 1(a). Several species in the dashed box area are not detected in the in-situ DRIFTS spectra due to the high number of oxygen vacancies in CeO$_2$-S that can rapidly oxidize the intermediates. Styrene is initially adsorbed on the surface through the interaction between vinyl and surface adsorbed oxygen. After the cleavage of the C═C double bond and dehydrogenation, benzyl alcohol species are formed. With the participation of gaseous oxygen, benzyl alcohol species are gradually converted into benzoate species on the catalyst surface. Therefore, oxygen vacancies and surface adsorbed oxygen play a crucial role in the formation of benzoate species. Finally, further oxidation occurs to form CO$_2$ and H$_2$O final products. At the same time, lattice oxygen was consumed to produce oxygen vacancies, and Ce^{4+} was reduced to Ce^{3+}. With the adsorption and activation of gaseous O$_2$ on the surface oxygen vacancies to form reactive oxygen species, Ce^{3+} was gradually oxidized to form Ce^{4+}. Finally, the active oxygen combined with Ce^{4+} to form lattice oxygen and the oxygen vacancies were filled. This phenomenon is most evident for the CeO$_2$-S catalyst (Fig. S20). CeO$_2$-S has the highest oxygen vacancy concentration causing the largest lattice distortion which can promote the breaking of the aromatic ring to increase the reaction rate. Moreover, Styrene-TPSR experiments were carried out using ^{18}O$_2$ isotope tracing, and the relationship between the conversion reaction rate of styrene to CO$_2$ and the surface adsorbed oxygen were also analyzed, the more details and results were shown in Supplementary information and Fig. S21. In conclusion, the above-described characterizations (Styrene-TPD, Styrene-TPSR, XPS, in situ DRIFTS, ^{18}O$_2$ isotope tracing experiment and the analysis of the relationship between the conversion reaction rate of styrene and the surface adsorbed oxygen) further demonstrated that the styrene oxidation on CeO$_2$ catalysts with different morphologies follows the Langmuir-Hinshelwood (L-H) mechanism due to the role of the surface adsorbed oxygen as reactive oxygen species involved in the catalytic oxidation of styrene at low temperature [13]. As the temperature increases, the lattice oxygen is gradually activated and participates in the oxidation via the Mars-van Krevelen (MVK) mechanism [48].

3.5. DFT theoretical calculations analysis

From the perspective of theoretical calculation, DFT calculations can be further used to explore the adsorption energy of different crystal planes ((111), (100) and (110)) of CeO$_2$ for oxygen, styrene and important intermediate benzoic acid. By comparison (Fig. S22(a)–(c)), the corresponding optimized adsorption structures are shown in Fig. S23. The adsorption energy of oxygen, styrene and benzoic acid over (111), (100) and (110) are shown in Scheme 1(b), the adsorption energy of oxygen, styrene and benzoic acid on CeO$_{2-x}$-(111) are −2.03, −1.95 and −1.56 eV respectively, which are larger negative than CeO$_{2-x}$-(100) and CeO$_{2-x}$-(110). The result indicates that the CeO$_{2-x}$-(111) crystal plane is beneficial to the adsorption of O$_2$, styrene and benzoic acid, which are consistent with the results of O$_2$-TPD, Styrene-TPD and Styrene-TPSR. To further demonstrate the role of oxygen vacancies, the absence of oxygen vacancies in the crystal plane of CeO$_2$-(111) was further discussed (Fig. S22(d), (e)). The defect-rich CeO$_{2-x}$-(111) has a significantly greater adsorption energy for styrene than CeO$_2$-(111). Therefore, the CeO$_{2-x}$-(111) facilitates the adsorption of styrene, and
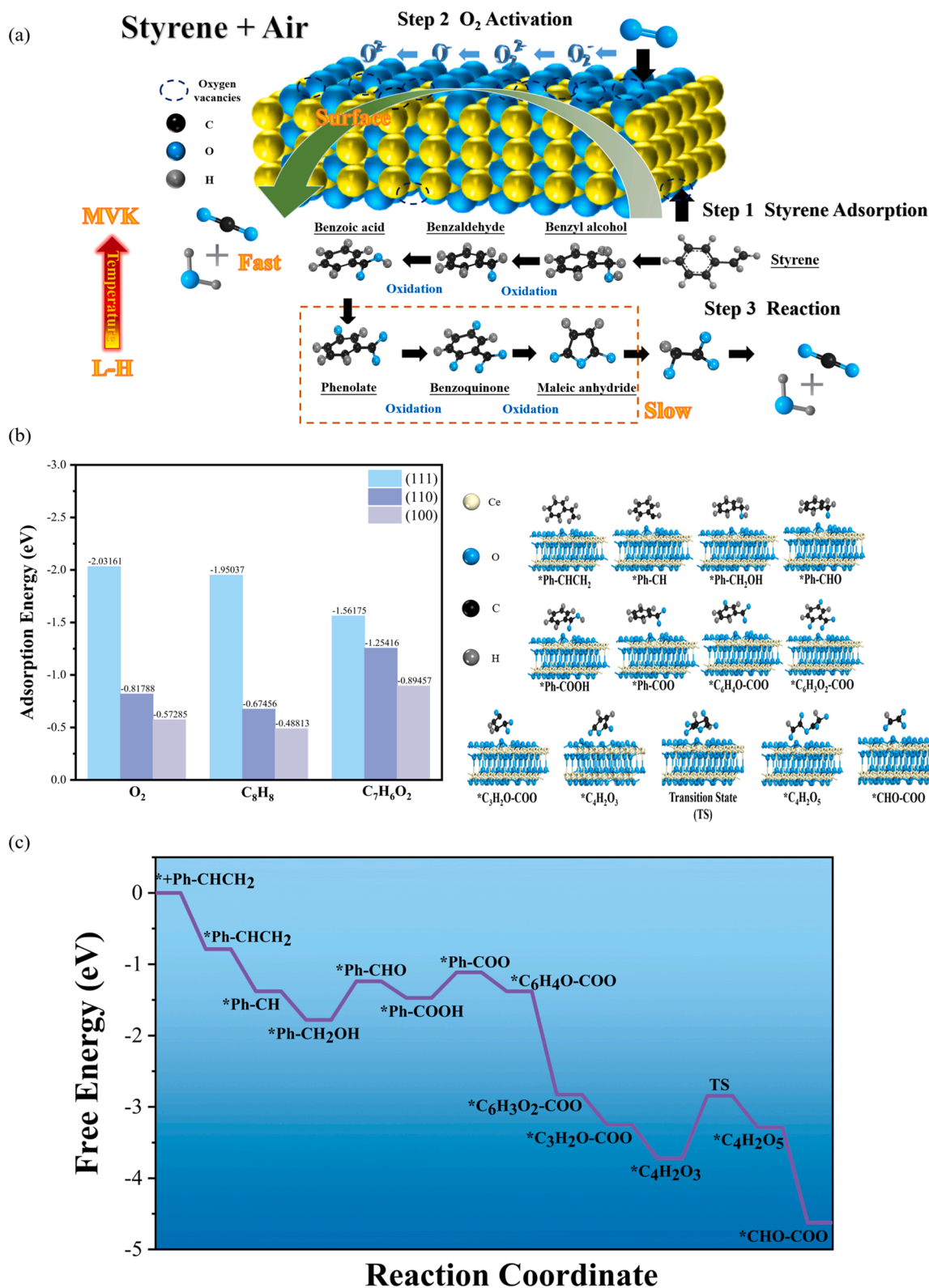
Scheme 1. (a) The possible adsorption and oxidation mechanisms of styrene over CeO$_2$-S catalyst; (b) Adsorption energy of oxygen molecules, styrene and benzoate on the (111), (100) and (110) crystal planes of CeO$_2$; (c) Energy pathways and structural evolution of intermediates for the catalytic oxidation of styrene on the CeO$_{2-x}$-(111) crystal plane.

more surface adsorbed oxygen will be formed on the surface of catalyst. Further analysis, based on the results of Styrene-TPD and Styrene-TPSR, reveal that the strong and suitable adsorption energy of oxygen and styrene contributes to the oxidation of styrene. Based on in-situ DRIFTS results, benzoate species is an important intermediate in the catalytic oxidation of styrene, the enhanced and favorable adsorption energy of benzoate species also facilitates the further oxidation of benzoate species to final products CO$_2$ and H$_2$O. Consequently, this is the reason why the

CeO$_2$-S catalyst, which mainly exposes the (111) crystal plane, has the best catalytic activity.

Furthermore, the energy pathways and structural evolution of intermediates for the catalytic oxidation of styrene on the CeO$_{2-x}$-(111) crystal plane (Scheme 1(c)) were also used to demonstrate the related mechanism analysis based on the in-situ DRIFTS. At low temperature, styrene is first adsorbed on the surface of CeO$_{2-x}$-(111), and the free energy reduces -0.79 eV. And the styrene is broken the C═C of the vinyl group under the activation of the surface adsorbed oxygen (O$_2^-$ and O$^-$), and to from the benzyl alcohol (*C$_6$H$_5$-CH$_2$OH), accompanied by a free energy decrease of −0.99 eV. And then benzyl alcohol is further oxidized with the involvement of surface adsorbed oxygen to form benzaldehyde (*C$_6$H$_5$-CHO), and further oxidized to benzoate species (*C$_6$H$_5$-COOH). This process requires activation barrier of 0.54 eV and accompanying with a free energy decrease of 0.23 eV. With the deep oxidation of styrene, more active oxygen species are required to participate in the reaction. Thus, the lattice oxygen in the CeO$_2$ participate in the oxidation reaction, and both the gas phase oxygen and the lattice oxygen will be activated and become surface adsorbed oxygen, which is active oxygen species on the oxygen vacancies. Then the active oxygen species is attached to the aromatic ring to form phenolate species (*C$_6$H$_4$O-COO), with a free energy increase of 0.09 eV. Next, the second oxygen is attached to the other side of aromatic ring to produce benzoquinone species (*C$_6$H$_3$O$_2$-COO), along with a free energy decrease of −1.45 eV. Then maleic anhydride species (*C$_4$H$_2$O$_3$) are generated by oxidation of active species (−0.89 eV). These processes are spontaneous in terms of energy. Before the final products (CO$_2$ and H$_2$O) are formed, it is worth noting that benzyl alcohol is oxidized to benzaldehyde, as well as the destruction of benzoate species and maleic anhydride, the free energy of these processes shows an upward trend. Combined with the analysis of in-situ DRIFTS results, the rapid decomposition of maleic

anhydride is conducive to the progress of the reaction. Indeed, the destruction of maleic anhydride needs to overcome the energy barrier of 0.88 eV. After the maleic anhydride species are decomposed, it is easy to form an acetate species (*CHO-COO), which is then oxidized to final products CO$_2$ and H$_2$O.

3.6. Stability and water resistance tests

To explore the long-term stability of the best activity CeO$_2$-S catalyst, on-steam styrene catalytic degradation was tested for the CeO$_2$-S sample at 225 °C. As shown in Fig. 9(a), the styrene degradation performance of CeO$_2$-S was maintained at almost 100% for 65 h, and CO$_2$ production remained stable. The catalytic resistance to H$_2$O (7 vol% or 20 vol%) is shown in Fig. 9(b). According to the relevant literatures, water is the main product of the styrene catalytic oxidation, and has a negative effect on the catalytic reaction due to competitive adsorption on the active sites [25,36]. A certain volume of water was introduced in the stability test of styrene to investigate the effect of water vapor on the activity of CeO$_2$-S catalyst, and the results are shown in Fig. 9(b). It is observed that when a 7 vol% water vapor is introduced into the reaction system, the styrene degradation conversion is barely affected. And when the water vapor content is increased to 20 vol%, the styrene degradation drops to 98% with a 2% lossy. Once the water vapor is turned off, the styrene degradation can still return to almost 100%. This phenomenon suggests that the competitive adsorption between styrene and water molecules is not significant, and the CeO$_2$-S catalyst shows good water resistance. Fig. 9(c) shows the styrene degradation and yield of CO$_2$ over CeO$_2$-S catalyst in the presence of 7 vol% water vapor from 100 to 350 °C. The styrene degradation is almost unaffected regardless of the absence and presence of water vapor, which is consistent with the results of stability tests. The different adsorption configurations maybe have different
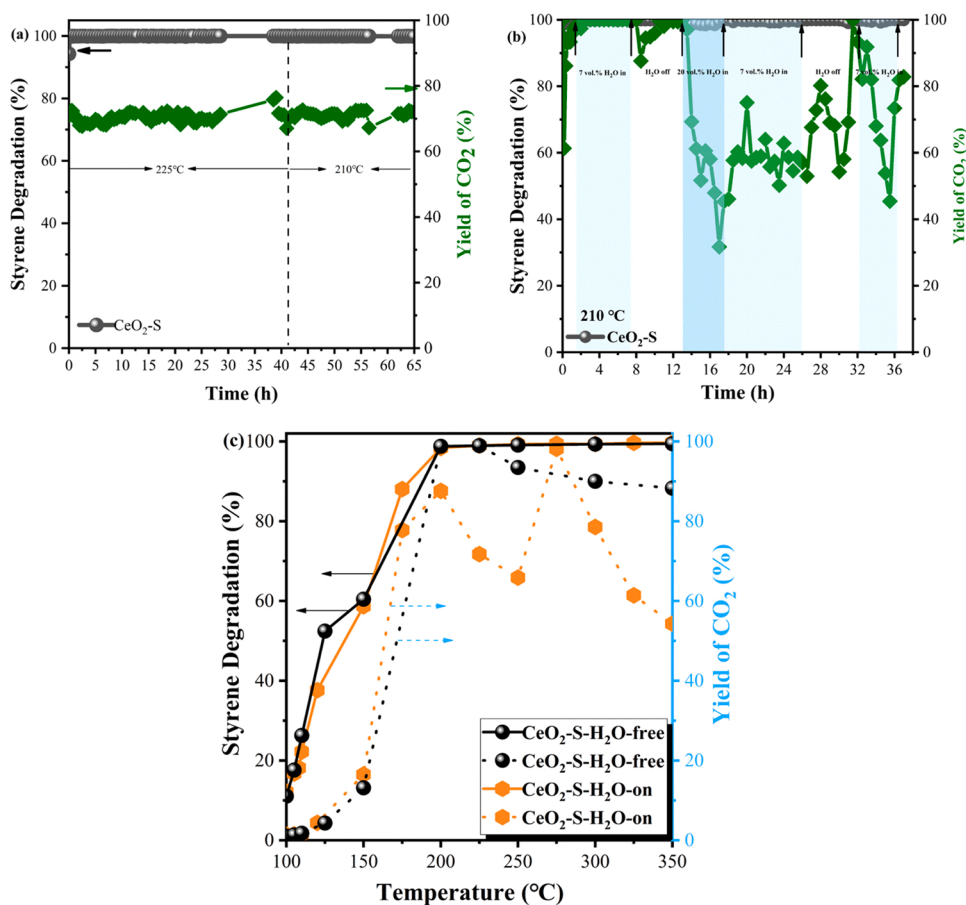

Fig. 9. (a) Catalyst stability test over CeO$_2$-S for 65 h (reaction condition: 400 ppm styrene +25% air with a total flow rate of 50 mL min^{-1}, 0.20 g catalyst under WHSV =15,000 mL/(g·h) at 225 °C and 210 °C). (b) Water resistance performance switch of with water and without water over CeO$_2$-S catalyst for 38 h. Reaction condition: 400 ppm styrene + 25% air + balanced N$_2$, total flow rate of 50 mL min^{-1}, besides, 7 vol% / 20 vol% water vapor was involved, 210 °C. (c) Catalytic performance of styrene degradation over CeO$_2$-S catalysts without H$_2$O and with 7 vol% H$_2$O vapor.

sensitivities to water, and the styrene is adsorbed to the surface of CeO_2 catalyst in a parallel molecular configuration (Figure S22(c)) is more energy-preferential. Therefore, styrene is not sensitive to the water vapor environment. It is worth noting that the presence of water vapor affects the CO_2 yield and leads to a decrease in CO_2 yield. Thus, the introduction of water vapor into the catalytic oxidation process of styrene, it will have a negatively effect on the complete mineralization rate of styrene. The possible reason for this phenomenon is that the addition of water and the generated CO_2 will further generate carbonates [54]. Another reason could be that the addition of water vapor is not conducive to the adsorption and activation of CeO_2-S on gas-phase oxygen, which does not facilitate the deep oxidation of styrene to CO_2.

4. Conclusions

In summary, CeO_2 catalysts with four different morphologies were synthesized and their catalytic oxidation performance for styrene oxidation was investigated. According to the characterization results, the lattice distortion is the key factor to form oxygen vacancies on CeO_2 catalysts with four different morphologies. The oxygen vacancies not only can adsorb and activate more oxygen to produce surface adsorbed oxygen, but also adsorb more styrene. Among all samples, CeO_2-S showed the highest catalytic activity (T_{50} =133 °C and T_{90} =184 °C) due to its highest oxygen vacancy concentration. It is noted that linear relationships were found between the oxygen vacancy concentration and the amount of surface adsorbed oxygen species, and between the amount of surface adsorbed oxygen species and the styrene oxidation rate. These results suggest that surface adsorbed oxygen species are the active sites for styrene oxidation, and are responsible for the superior activity of CeO_2-S. Moreover, the in-situ DRIFTS tests provide clear evidence that the styrene oxidation rate of CeO_2-S is higher than those of the other samples due to its highest concentration of oxygen vacancies, which promote the rapid and deep oxidation of intermediate products (maleic anhydride) to the CO_2 and H_2O final products. Isotope tracing experiment further verified the mechanism of styrene catalytic oxidation, which change from L-H mechanism (low temperature) to MVK mechanism (high temperature). DFT theoretical calculations demonstrate the role of defects and crystal planes in the catalytic oxidation of styrene, and also reveal the intermediates of the catalytic oxidation of styrene on the CeO_2-S (111). The results show that the decomposition of maleic anhydride is an important step to control the reaction rate. Additionally, CeO_2-S catalyst shows excellent catalytic stability and tolerance to the presence of water vapor. This study provides the understanding between the lattice distortion and oxygen vacancy, identifies the role of oxygen vacancies, and demonstrates the mechanism of styrene degradation.

CRediT authorship contribution statement

Ying Zhang: Conceptualization, Methodology, Data analysis, Software, Investigation, Writing & Editing. **Jichang Lu:** Resources, Writing – review & editing, Formal analysis. **Liming Zhang:** Validation, Visualization. **Te Fu:** Validation, Formal analysis, Software, Data analysis. **Jin Zhang:** Resources. **Xing Zhu:** Resources. **Xiaoya Gao:** Writing – review & editing. **Dedong He:** Writing – review & editing. **Yongming Luo:** Resources, Writing – review & editing, Supervision, Data curation. **Dionysios D. Dionysiou:** Writing – review & editing. **Wenjie Zhu:** Resources, Formal analysis, Writing – review & editing, Supervision, Data curation.

Declaration of Competing Interest

The authors declare that they have no known competing financial interests or personal relationships that could have appeared to influence the work reported in this paper.

Appendix A. Supplementary material

Supplementary data associated with this article can be found in the online version at doi:10.1016/j.apcatb.2022.121249.

References

[1] B. Solsona, T. García, R. Sanchis, M.D. Soriano, M. Moreno, E. Rodríguez-Castellón, S. Agouram, A. Dejoz, J.M.López Nieto, Total oxidation of VOCs on mesoporous iron oxide catalysts: soft chemistry route versus hard template method, Chem. Eng. J. 290 (2016) 273–281, https://doi.org/10.1016/j.cej.2015.12.109.

[2] Y. Guo, M. Wen, G. Li, T. An, Recent advances in VOC elimination by catalytic oxidation technology onto various nanoparticles catalysts: a critical review, Appl. Catal. B Environ. 281 (2020) 119447, https://doi.org/10.1016/j.apcatb.2020.119447.

[3] J. Chen, Z. He, Y. Ji, G. Li, T. An, W. Choi, OH radicals determined photocatalytic degradation mechanisms of gaseous styrene in TiO_2 system under 254 nm versus 185 nm irradiation: combined experimental and theoretical studies, Appl. Catal. B Environ. 257 (2019), 117912, https://doi.org/10.1016/j.apcatb.2019.117912.

[4] H. Zhang, K. Li, L. Li, L. Liu, X. Meng, T. Sun, J. Jia, M. Fan, High efficient styrene mineralization through novel NiO-TiO2-Al2O3 packed pre-treatment/treatment/post-treatment dielectric barrier discharge plasma, Chem. Eng. J. 343 (2018) 759–769, https://doi.org/10.1016/j.cej.2018.03.057.

[5] J. Chen, Z. He, Y. Ji, G. Li, T. An, W. Choi, OH radicals determined photocatalytic degradation mechanisms of gaseous styrene in TiO_2 system under 254 nm versus 185 nm irradiation: combined experimental and theoretical studies, Appl. Catal. B Environ. 257 (2019), 117912, https://doi.org/10.1016/j.apcatb.2019.117912.

[6] G. Li, K. Shen, L. Wang, Y. Zhang, H. Yang, P. Wu, B. Wang, S. Zhang, Synergistic degradation mechanism of chlorobenzene and NOx over the multi-active center catalyst: the role of NO2, Brønsted acidic site, oxygen vacancy, Appl. Catal. B Environ. 286 (2021), 119865, https://doi.org/10.1016/j.apcatb.2020.119865.

[7] J. Wan, J. Lin, X. Guo, T. Wang, R. Zhou, Morphology effect on the structure-activity relationship through Rh/CeO2-ZrO2 catalysts, Chem. Eng. J. 368 (2019) 719–729, https://doi.org/10.1810/j.cej.2019.03.016.

[8] J. Kong, Z. Xiang, G. Li, T. An, Introduce oxygen vacancies into CeO_2 catalyst for enhanced coke resistance during photothermocatalytic oxidation of typical VOCs, Appl. Catal. B Environ. 269 (2020), 118755, https://doi.org/10.1016/j.apcatb.2020.118755.

[9] X. Zhang, F. Bi, Z. Zhu, Y. Yang, S. Zhao, J. Chen, X. Lv, Y. Wang, J. Xu, N. Liu, The promoting effect of H_2O on rod-like $MnCeO_x$ derived from MOFs for toluene oxidation: a combined experimental and theoretical investigation, Appl. Catal. B Environ. 297 (2021), 120393, https://doi.org/10.1016/j.apcatb.2021.120393.

[10] S. Rong, T. He, P. Zhang, Self-assembly of MnO_2 nanostructures into high purity three-dimensional framework for high efficiency formaldehyde mineralization, Appl. Catal. B Environ. 267 (2020), 118375, https://doi.org/10.1016/j.apcatb.2019.118375.

[11] F. Dong, W. Han, Y. Guo, W. Han, Z. Tang, $CeCoO_x$-MNS catalyst derived from three-dimensional mesh nanosheet Co-based metal–organic frameworks for highly efficient catalytic combustion of VOCs, Chem. Eng. J. 405 (2021) 126948, https://doi.org/10.1016/j.cej.2020.126948.

[12] J. Lu, J. Zhong, Q. Ren, J. Li, L. Song, S. Mo, M. Zhang, P. Chen, M. Fu, D. Ye, Construction of Cu-Ce interface for boosting toluene oxidation: study of Cu-Ce interaction and intermediates identified by in situ DRIFTS, Chin. Chem. Lett. (2021) 6372, https://doi.org/10.1016/j.cclet.2021.05.029.

[13] Z. Jiang, M. Jing, X. Feng, J. Xiong, C. He, M. Douthwaite, L. Zheng, W. Song, J. Liu, Z. Qu, Stabilizing platinum atoms on CeO_2 oxygen vacancies by metal-support interaction induced interface distortion: mechanism and application, Appl. Catal. B Environ. 278 (2020) 119304, https://doi.org/10.1016/j.apcatb.2020.119304.

[14] Y. Shi, Z. Li, J. Wang, R. Zhou, Synergistic effect of Pt/Ce and USY zeolite in Pt-based catalysts with high activity for VOCs degradation, Appl. Catal. B Environ. 286 (2020), 119936, https://doi.org/10.1016/j.apcatb.2021.119936.

[15] Z. Zhang, R. Li, M. Wang, Y. Li, Y. Tong, P. Yang, Y. Zhu, Two steps synthesis of CeTiOx oxides nanotube catalyst: enhanced activity, resistance of SO_2 and H_2O for low temperature NH_3-SCR of NO_x, Appl. Catal. B Environ. 282 (2021) 119542, https://doi.org/10.1016/j.apcatb.2020.119542.

[16] J. Deng, W. Song, L. Chen, L. Wang, M. Jing, Y. Ren, Z. Zhao, J. Liu, The effect of oxygen vacancies and water on HCHO catalytic oxidation over Co_3O_4 catalyst: a combination of density functional theory and microkinetic study, Chem. Eng. J. 355 (2019) 540–550, https://doi.org/10.1016/j.cej.2018.08.195.

[17] M. Sun, X. Wang, Z. Chen, M. Murugananthan, Y. Chen, Y. Zhang, Stabilized oxygen vacancies over heterojunction for highly efficient and exceptionally durable VOCs photocatalytic degradation, Appl. Catal. B Environ. 273 (2020), 119061, https://doi.org/10.1016/j.apcatb.2020.119061.

[18] M. Wu, S. Chen, W. Xiang, Oxygen vacancy induced performance enhancement of toluene catalytic oxidation using LaFeO₃ perovskite oxides, Chem. Eng. J. 387 (2020), 124101, https://doi.org/10.1016/j.cej.2020.124101.

[19] L. Chen, Y. Liu, X. Fang, Y. Cheng, Simple strategy for the construction of oxygen vacancies on α-MnO₂ catalyst to improve toluene catalytic oxidation, J. Hazard. Mater. 409 (2021), 125020, https://doi.org/10.1016/j.jhazmat.2020.125020.

[20] S. Zhang, C.R. Chang, Z.Q. Huang, J. Li, Z. Wu, Y. Ma, Z. Zhang, Y. Wang, Y. Qu, High catalytic activity and chemoselectivity of sub-nanometric Pd clusters on porous nanorods of CeO₂ for hydrogenation of nitroarenes, J. Am. Chem. Soc. 138 (2016) 2629–2637, https://doi.org/10.1021/jacs.5b11413.

[21] F. Jiang, S. Wang, B. Liu, J. Liu, L. Wang, Y. Xiao, Y. Xu, X. Liu, Insights into the influence of CeO₂ crystal facet on CO₂ hydrogenation to methanol over Pd/CeO₂ catalysts, ACS Catal. 10 (2020) 11493–11509, https://doi.org/10.1021/acscatal.0c03324.

[22] X. Zhao, C. Pei, X. Chang, S. Chen, R. Liu, Z.-J. Zhao, R. Mu, J. Gong, FeO₆ octahedral distortion activates lattice oxygen in perovskite ferrite for methane partial oxidation coupled with CO₂ splitting, J. Am. Chem. Soc. 142 (2020) 11540–11549, https://doi.org/10.1021/jacs.0c04643.

[23] Q. Zou, Y. Zhao, X. Jin, J. Fang, D. Li, K. Li, J. Lu, Y. Luo, Ceria-nano supported copper oxide catalysts for CO preferential oxidation: Importance of oxygen species and metal-support interaction, Appl. Surf. Sci. 494 (2019) 1166–1176, https://doi.org/10.1016/j.apsusc.2019.07.210.

[24] Z. Xu, W. Yang, W. Si, J. Chen, Y. Peng, J. Li, A novel γ-like MnO₂ catalyst for ozone decomposition in high humidity conditions, J. Hazard. Mater. 420 (2021), 126641, https://doi.org/10.1016/j.jhazmat.2021.126641.

[25] P. Wang, J. Wang, X. An, J. Shi, W. Shangguan, X. Hao, G. Xu, B. Tang, A. Abudula, G. Guan, Generation of abundant defects in Mn-Co mixed oxides by a facile agar-gel method for highly efficient catalysis of total toluene oxidation, Appl. Catal. B Environ. 282 (2021) 119560, https://doi.org/10.1016/j.apcatb.2020.119560.

[26] Z. Xiao, C. Wu, L. Wang, J. Xu, Q. Zheng, L. Pan, J. Zou, X. Zhang, G. Li, Boosting hydrogen production from steam reforming of ethanol on nickel by lanthanum doped ceria, Appl. Catal. B Environ. 286 (2021), 119884, https://doi.org/10.1016/j.apcatb.2021.119884.

[27] F. Hu, J. Chen, Y. Peng, H. Song, K. Li, J. Li, Novel nanowire self-assembled hierarchical CeO₂ microspheres for low temperature toluene catalytic combustion, Chem. Eng. J. 331 (2018) 424–434, https://doi.org/10.1016/j.cej.2017.08.110.

[28] W. Zhang, X.L. Ma, H. Xiao, M. Lei, J. Li, Mechanistic investigations on thermal hydrogenation of CO₂ to methanol by nanostructured CeO₂(100): the crystal-plane effect on catalytic reactivity, J. Phys. Chem. C 123 (2019) 11763–11771, https://doi.org/10.1021/acs.jpcc.9b02120.

[29] X. Zheng, Y. Li, L. Zhang, L. Shen, Y. Xiao, Y. Zhang, C. Au, L. Jiang, Insight into the effect of morphology on catalytic performance of porous CeO₂ nanocrystals for H₂S selective oxidation, Appl. Catal. B Environ. 252 (2019) 98–110, https://doi.org/10.1016/j.apcatb.2019.04.011.

[30] F. Wang, C. Li, X. Zhang, M. Wei, D.G. Evans, X. Duan, Catalytic behavior of supported Ru nanoparticles on the {100}, {110}, and {111} facet of CeO₂, J. Catal. 329 (2015) 177–186, https://doi.org/10.1016/j.jcat.2015.05.014.

[31] L. Torrente-Murciano, A. Gilbank, B. Puertolas, T. Garcia, B. Solsona, D. Chadwick, Shape-dependency activity of nanostructured CeO₂ in the total oxidation of polycyclic aromatic hydrocarbons, Appl. Catal. B Environ. 132–133 (2013) 116–122, https://doi.org/10.1016/j.apcatb.2012.10.030.

[32] Z. Feng, Q. Ren, R. Peng, S. Mo, M. Zhang, M. Fu, L. Chen, D. Ye, Effect of CeO₂ morphologies on toluene catalytic combustion, Catal. Today 332 (2019) 177–182, https://doi.org/10.1016/j.cattod.2018.06.039.

[33] F. Liu, H. Zhou, Z. Pan, Y. Liu, G. Yao, Y. Guo, B. Lai, Degradation of sulfamethoxazole by cobalt-nickel powder composite catalyst coupled with peroxymonosulfate: performance, degradation pathways and mechanistic consideration, J. Hazard. Mater. 400 (2020), 123322, https://doi.org/10.1016/j.jhazmat.2020.123322.

[34] H. He, X. Lin, S. Li, Z. Wu, J. Gao, J. Wu, W. Wen, D. Ye, M. Fu, The key surface species and oxygen vacancies in MnOₓ(0.4)-CeO₂ toward repeated soot oxidation, Appl. Catal. B Environ. 223 (2018) 134–142, https://doi.org/10.1016/j.apcatb.2017.08.084.

[35] L. Ma, D. Wang, J. Li, B. Bai, L. Fu, Y. Li, Ag/CeO₂ nanospheres: efficient catalysts for formaldehyde oxidation, Appl. Catal. B Environ. 148–149 (2014) 36–43, https://doi.org/10.1016/j.apcatb.2013.10.039.

[36] Y. Xie, J. Wu, G. Jing, H. Zhang, S. Zeng, X. Tian, X. Zou, J. Wen, H. Su, C. Zhong, P. Cui, Structural origin of high catalytic activity for preferential CO oxidation over CuO/CeO₂ nanocatalysts with different shapes, Appl. Catal. B Environ. 239 (2018) 665–676, https://doi.org/10.1016/j.apcatb.2018.08.066.

[37] H. Li, C.-Y. Wu, Y. Li, J. Zhang, Superior activity of MnOₓ-CeO₂/TiO₂ catalyst for catalytic oxidation of elemental mercury at low flue gas temperatures, Appl. Catal. B Environ. 111–112 (2012) 381–388, https://doi.org/10.1016/j.apcatb.2011.10.021.

[38] L. Wang, Y. Wang, Y. Zhang, Y. Yu, H. He, X. Qin, B. Wang, Shape dependence of nanoceria on complete catalytic oxidation of o-xylene, Catal. Sci. Technol. 6 (2016) 4840–4848, https://doi.org/10.1039/C6CY00180G.

[39] A.J. Medford, A. Vojvodic, J.S. Hummelshøj, J. Voss, F. Abild-Pedersen, F. Studt, T. Bligaard, A. Nilsson, J.K. Nørskov, From the Sabatier principle to a predictive theory of transition-metal heterogeneous catalysis, J. Catal. 328 (2015) 36–42, https://doi.org/10.1016/j.jcat.2014.12.033.

[40] S. Mo, Q. Zhang, J. Li, Y. Sun, Q. Ren, S. Zou, Q. Zhang, J. Lu, M. Fu, D. Mo, J. Wu, H. Huang, D. Ye, Highly efficient mesoporous MnO₂ catalysts for the total toluene oxidation: oxygen-vacancy defect engineering and involved intermediates using in situ DRIFTS, Appl. Catal. B Environ. 264 (2020), 118464, https://doi.org/10.1016/j.apcatb.2019.118464.

[41] L. Zhao, Z. Zhang, Y. Li, X. Leng, T. Zhang, F. Yuan, X. Niu, Y. Zhu, Synthesis of CeₐMnOₓ hollow microsphere with hierarchical structure and its excellent catalytic performance for toluene combustion, Appl. Catal. B Environ. 245 (2019) 502–512, https://doi.org/10.1016/j.apcatb.2019.01.005.

[42] C. Chizallet, G. Costentin, M. Che, F. Delbecq, P. Sautet, Infrared characterization of hydroxyl groups on MgO: a periodic and cluster density functional theory study, J. Am. Chem. Soc. 129 (2007) 6442–6452, https://doi.org/10.1021/ja068720e.

[43] A. Davó-Quiñonero, M. Navlani-García, D. Lozano-Castelló, A. Bueno-López, J. A. Anderson, Role of hydroxyl groups in the preferential oxidation of CO over copper oxide–cerium oxide catalysts, ACS Catal. 6 (2016) 1723–1731, https://doi.org/10.1021/acscatal.5b02741.

[44] Q. Zhang, S. Mo, J. Li, Y. Sun, M. Zhang, P. Chen, M. Fu, J. Wu, L. Chen, D. Ye, In situ DRIFT spectroscopy insights into the reaction mechanism of CO and toluene co-oxidation over Pt-based catalysts, Catal. Sci. Technol. 9 (2019) 4538–4551, https://doi.org/10.1039/C9CY00751B.

[45] J. Huang, R. Fang, Y. Sun, J. Li, F. Dong, Efficient α-MnO₂ with (2 1 0) facet exposed for catalytic oxidation of toluene at low temperature: a combined in-situ DRIFTS and theoretical investigation, Chemosphere 263 (2021), 128103, https://doi.org/10.1016/j.chemosphere.2020.128103.

[46] X. Yang, X. Yu, M. Jing, W. Song, J. Liu, M. Ge, Defective MnxZr₁₋ₓO₂ solid solution for the catalytic oxidation of toluene: insights into the oxygen vacancy contribution, ACS Appl. Mater. Interfaces 11 (2019) 730–739, https://doi.org/10.1021/acsami.8b17062.

[47] X. Chen, X. Chen, E. Yu, S. Cai, H. Jia, J. Chen, P. Liang, In situ pyrolysis of Ce-MOF to prepare CeO₂ catalyst with obviously improved catalytic performance for toluene combustion, Chem. Eng. J. 344 (2018) 469–479, https://doi.org/10.1016/j.cej.2018.03.091.

[48] X. Wan, L. Wang, S. Gao, X. Lang, L. Wang, T. Zhang, A. Dong, W. Wang, Low-temperature removal of aromatics pollutants via surface labile oxygen over Mn-based mullite catalyst SmMn₂O₅, Chem. Eng. J. 410 (2021), 128305, https://doi.org/10.1016/j.cej.2020.128305.

[49] L. Ma, C.Y. Seo, X. Chen, K. Sun, J.W. Schwank, Indium-doped Co₃O₄ nanorods for catalytic oxidation of CO and C₃H₆ towards diesel exhaust, Appl. Catal. B Environ. 222 (2018) 44–58, https://doi.org/10.1016/j.apcatb.2017.10.001.

[50] J. Zhong, Y. Zeng, M. Zhang, W. Feng, D. Xiao, J. Wu, P. Chen, M. Fu, D. Ye, Toluene oxidation process and proper mechanism over Co₃O₄ nanotubes: investigation through in-situ DRIFTS combined with PTR-TOF-MS and quasi in-situ XPS, Chem. Eng. J. 397 (2020), 125375, https://doi.org/10.1016/j.cej.2020.125375.

[51] L. Yang, F. Zhang, T. Endo, T. Hirotsu, Microstructure of maleic anhydride grafted polyethylene by high-resolution solution-state NMR and FTIR spectroscopy, Macromolecules 36 (2003) 4709–4718, https://doi.org/10.1021/ma020527r.

[52] P. Sun, W. Wang, X. Dai, X. Weng, Z. Wu, Mechanism study on catalytic oxidation of chlorobenzene over MnₓCe₁₋ₓO₂/H-ZSM5 catalysts under dry and humid conditions, Appl. Catal. B Environ. 198 (2016) 389–397, https://doi.org/10.1016/j.apcatb.2016.05.076.

[53] C. Zhou, H. Zhang, Z. Zhang, L. Li, Improved reactivity for toluene oxidation on MnOₓ/CeO₂-ZrO₂ catalyst by the synthesis of cubic-tetragonal interfaces, Appl. Surf. Sci. 539 (2021), 148188, https://doi.org/10.1016/j.apsusc.2020.148188.

[54] C. Li, Y. Sakata, T. Arai, K. Domen, K. Maruya, T. Onishi, Adsorption of carbon monoxide and carbon dioxide on cerium oxide studied by Fourier-transform infrared spectroscopy, J. Chem. Soc. Faraday Trans. I 85 (1989) 1451–1461, https://doi.org/10.1039/F19898501451.